Deformation and evolution of solar wind discontinuities through their interactions with the Earth's bow shock

K. Keika,[1,2] R. Nakamura,[1] W. Baumjohann,[1] V. Angelopoulos,[3] K. Kabin,[4] K. H. Glassmeier,[5,6] D. G. Sibeck,[7] W. Magnes,[1] H. U. Auster,[5] K. H. Fornaçon,[5] J. P. McFadden,[8] C. W. Carlson,[8] E. A. Lucek,[9] C. M. Carr,[9] I. Dandouras,[10] and R. Rankin[4]

Received 13 June 2008; revised 12 May 2009; accepted 26 May 2009; published 17 September 2009.

[1] The present study examines the interaction of solar wind discontinuities with the Earth's bow shock, using multipoint observations in the magnetosheath by Time History of Events and Macroscale Interactions During Substorms (THEMIS), Cluster, and Double Star TC1. We focus on the deformation and evolution of two discontinuities observed on 21 June 2007, one of which involves a density increase and a magnetic field decrease, while the other is accompanied by a density decrease and a magnetic field increase. In the magnetosheath, the discontinuities are deformed into a concave shape; that is, the normal is inclined toward dusk (dawn) on the dawnside (duskside). The density-increase (-decrease) discontinuity is being compressed (expanded) as it propagates in the magnetosheath. We conclude that the compression (expansion) is due to antisunward (sunward) motion of the bow shock which is initiated or enhanced by the impact of the discontinuity on the bow shock. The steepening of B_z reversal followed by an overshoot of the total magnetic field, which appears at the trailing edge of the density-decrease discontinuity, is also discussed.

Citation: Keika, K., et al. (2009), Deformation and evolution of solar wind discontinuities through their interactions with the Earth's bow shock, *J. Geophys. Res.*, *114*, A00C26, doi:10.1029/2008JA013481.

1. Introduction

[2] Interactions of the solar wind with the Earth's magnetosphere generate the bow shock in front of the magnetopause, since the solar wind flows with supersonic and super-Alfvénic speed. The bow shock is formed on average at about 15 R_E and the solar wind is slowed down and heated after passing by the bow shock. Variations in solar wind properties such as the sonic and Alfvén Mach numbers change the bow shock location and strength, resulting in variations of the properties downstream of the bow shock [e.g., *Peredo et al.*, 1995; *Verigin et al.*, 2001].

[3] A solar wind shock or discontinuity involves sudden changes in the solar wind properties. When the shock or discontinuity hits the bow shock, new shocks and discontinuities are generated and propagate in the magnetosheath with different velocities [e.g., *Samsonov et al.*, 2007, and references therein]. The interaction between the bow shock and a discontinuity accompanied by a density increase has been examined theoretically [*Völk and Auer*, 1974; *Neubauer*, 1975; *Wu et al.*, 1993; *Maynard et al.*, 2008]. The bow shock is intensified and compressed through the interaction, creating a zone of enhanced compression downstream of the bow shock (i.e., in the magnetosheath), and then a new fast shock is produced [*Wu et al.*, 1993]. The interaction thus splits the bow shock into two fast shocks: the fast forward shock propagating in the magnetosheath ahead of the discontinuity and the bow shock itself behind the discontinuity. The bow shock after the interaction moves toward the Earth, until it reaches a new equilibrium position. When the density across the solar wind discontinuity decreases, the fast mode disturbance launched into the magnetosheath is a rarefaction wave and the bow shock moves sunward until it reaches a new equilibrium position.

[4] Recent MHD simulations have demonstrated that a fast forward shock generated through the interaction

[1]Space Research Institute, Austrian Academy of Sciences, Graz, Austria.
[2]Center for Solar-Terrestrial Research, New Jersey Institute of Technology, Newark, New Jersey, USA.
[3]Institute of Geophysics and Planetary Physics, University of California, Los Angeles, California, USA.
[4]Department of Physics, University of Alberta, Edmonton, Alberta, Canada.
[5]Institut für Geophysik und extraterrestrische Physik, Technische Universität Braunschweig, Braunschweig, Germany.
[6]Max Planck Institute of Solar System Research, Katlenburg-Lindau, Germany.
[7]NASA Goddard Space Flight Center, Greenbelt, Maryland, USA.
[8]Space Sciences Laboratory, University of California, Berkeley, California, USA.
[9]Space and Atmospheric Physics Group, Imperial College London, London, UK.
[10]Centre d'Etude Spatiale des Rayonnements, Université Paul Sabatier, UMR 5187, CNRS, Toulouse, France.

Copyright 2009 by the American Geophysical Union.
0148-0227/09/2008JA013481

between an interplanetary shock and the bow shock is deformed in the magnetosheath to assume a concave shape [*Koval et al.*, 2005; *Samsonov et al.*, 2006; *Šafránková et al.*, 2007]. *Přech et al.* [2008] confirmed such deformation, using data from multiple spacecraft in the duskside magnetosheath near the magnetopause. *Cable and Lin* [1998] and *Maynard et al.* [2007] demonstrated in their MHD simulations that a discontinuity propagating in the magnetosheath after its interaction with the bow shock is deformed. *Maynard et al.* [2007] also showed that a tangential discontinuity accompanied by a density decrease broadened with time as it moved across the magnetosheath. It was, however, impossible to discuss the broadening with observations, simply because there was only a single spacecraft available in the magnetosheath for the interval of their interest. Another case study by *Maynard et al.* [2008] analyzed interactions between a discontinuity with a density increase and the bow shock. They concluded that the discontinuity was being compressed as it propagated toward the magnetopause. The conclusion was derived from observations of velocity differences on both sides of the discontinuous surface pointed inward. Although they used data from the four spacecraft of Cluster, differences in magnetic field variations between the spacecraft were not clear. Studies on evolution of discontinuities do require multipoint observations by spacecraft widely distributed in the magnetosheath.

[5] On 21 June 2007, two discontinuities, one of which involved a density increase and a magnetic field decrease and the other of which was accompanied by a density decrease and a magnetic field increase, arrived at the bow shock, when multiple spacecraft were present in the magnetosheath covering much of the dayside magnetopause. Spacecraft from the Time History of Events and Macroscale Interactions During Substorms (THEMIS) mission [*Angelopoulos*, 2008] were located in the duskside magnetosheath; the Cluster spacecraft traveled in the dawnside magnetosheath; and the Double Star (DSP) TC1 spacecraft was in the magnetosheath near noon. This spacecraft configuration allows us for the first time to examine deformation of a discontinuity in the magnetosheath with in situ observations simultaneously made on both dawnside and duskside. The THEMIS spacecraft were lined up in the same orbit. They were consequently situated in the magnetosheath with the spacecraft separations of $<2\ R_E$ as the Cluster spacecraft were. Such configurations make it possible to follow the propagation of a discontinuity in the magnetosheath and therefore study how the discontinuity evolves as it moves across the magnetosheath.

[6] In this paper, we examine the deformation and evolution of the two discontinuities in the magnetosheath. After introducing data set used in the present study in section 2, we show the observations for the density-increase discontinuity in section 3 and those for the density-decrease discontinuity in section 4. The observations show compression (expansion) of the density-increase (-decrease) discontinuity. In section 5, we conduct a theoretical analysis for variations of plasma speed in the magnetosheath, taking into account the motion of the bow shock. We also demonstrate the results of an MHD simulation. After we devote discussion to the observations and the analyses in section 6, we summarize the conclusion in section 7.

2. Data Set

[7] The present study uses data from the following spacecraft: Wind, the Advanced Composition Explorer (ACE), THEMIS A, B, C, and E, Cluster 1, 2, and 3, and DSP/TC1. We use solar wind data from the Magnetic Field Investigation (MFI) [*Lepping et al.*, 1995] and the 3-D Plasma and Energetic Particle Investigation [*Lin et al.*, 1995] on Wind. Time resolution of the data is 3 s. From the magnetometer on ACE [*Smith et al.*, 1998], we use 16-s data. The THEMIS data used in this study are 3-s spin-fit magnetic field data obtained by the Fluxgate Magnetometer (FGM) [*Auster et al.*, 2008] and ion data with energies of $\sim$5 eV – 25 keV obtained by the Electro-Static Analyzer (ESA) plasma instrument [*McFadden et al.*, 2008]. ESA sweeps out 4π steradians every spin period (3s) and provides 3-s ion density and velocity data as the reduced distribution in which the angular distribution is reduced from 88 to 50 angles. DSP/TC1 provides 4-s magnetic field data obtained by the magnetometer [*Carr et al.*, 2005]. Cluster provides 4 s magnetic field data obtained by the FluxGate Magnetometer (FGM) [*Balogh et al.*, 2001]. The Hot Ion Analyzer (HIA) [*Rème et al.*, 2001] onboard Cluster detects ions with energies of 5 eV – 32 keV. We use 4-s ion density and velocity data provided by HIA on Cluster 1 and 3.

3. Density Increase Event

[8] A discontinuity, across which the density increases, arrived at Wind at 1141:20 UT and at ACE at about 1149 UT. It reached the bow shock around 1245 UT, when DSP/TC1, THEMIS A, and Cluster were located in the magnetosheath near noon, on the duskside and on the dawnside, respectively. Positions of the spacecraft are summarized in Figure 1 and Table 1.

3.1. Solar Wind Observations

[9] Figure 2 shows Wind and ACE observations in GSM coordinates at 1135–1200 UT. The magnetic field at Wind was changed between 1141:20 and 1143:20 UT; both times are indicated by black and red dashed lines, respectively. B_y increased from -8 to -2 nT and B_z increased from 3 to 7 nT. The field strength decreased from 8 to 6 nT. Density increased by a factor of $\sim$1.5 simultaneously, while the X component of velocity remains almost constant, and the dynamic pressure therefore increases. The thermal plasma pressure increased and the magnetic pressure decreased across the discontinuity. The magnetic field measured at ACE around 1150 UT shows a profile similar to that at Wind. B_y increased from -10 to -4 nT and B_z increased from 2 to 4 nT. The field strength decreased from 10 to 6 nT.

[10] We determine the nature of the discontinuity as follows. The minimum variance analysis (MVA) [*Sonnerup and Cahill*, 1967; *Sonnerup and Scheible*, 1998; *Song and Russell*, 1999], performed with the Wind data over the interval of 1140:00–1145:00 UT, gave a normal with a ratio of the intermediate-to-minimum eigenvalues of 8.0. The normal was $\phi = 178°$ and $\theta = -20°$, where ϕ and θ are

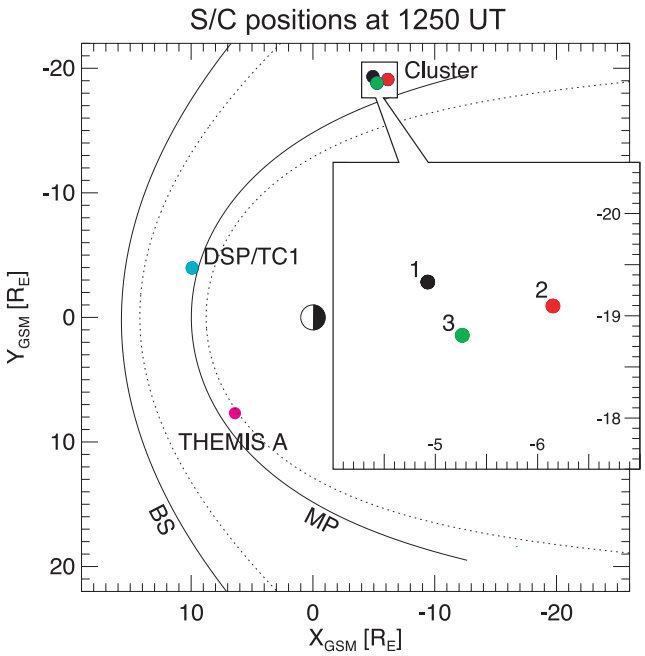

Figure 1. Spacecraft positions at 1250 UT. BS and MP denote the bow shock and the magnetopause, respectively. The locations of BS and MP are based on models by *Peredo et al.* [1995] and *Shue et al.* [1998]. Solid and dotted lines represent the locations before and after the arrival of the discontinuity; we choose input parameters for the models so that the model magnetopause locations can reproduce the THEMIS A magnetopause crossing.

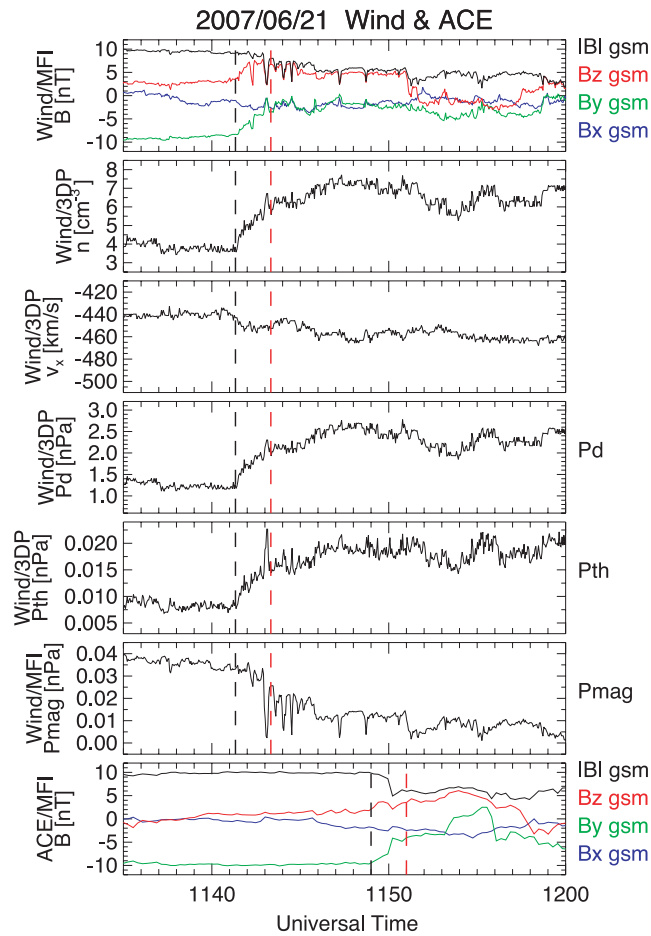

Figure 2. Solar wind observations by Wind and ACE between 1135 UT and 1200 UT. Black and red dashed lines indicate the leading and trailing edges of the discontinuity.

longitude and latitude in GSM coordinates. The normal component of **B** (B_n) was -0.092 ± 0.29 nT. The normal component of solar wind velocity (v_n) and the total pressure (p) were -420 km/s and 0.051 nPa, respectively, and they were nearly constant on both sides of the discontinuity; their standard deviations were 2.6 km/s and 0.0018 nPa, respectively. In calculating p, we assumed charge quasi-neutrality and equivalence of proton and electron temperatures and ignored the minor contribution from the alpha particles. Since B_n was small and v_n and p were nearly constant, the discontinuity is regarded as a tangential discontinuity. In fact, the estimated normal is quite close to that estimated from the cross product (CP) of **B** on both sides of the discontinuity ($\phi = -179°$ and $\theta = -26°$).

[11] We conducted two tests for tangential discontinuities described by *Neugebauer et al.* [1984] and *Neugebauer* [2006]: the ratio of B_n to $|\mathbf{B}|$ ($B_n/|\mathbf{B}|$) and the ratio of ΔB to $|\mathbf{B}|$ ($\Delta B/|\mathbf{B}|$), where ΔB is change in magnitude of **B** across the discontinuity. For a tangential discontinuity the first of these ratios should be smaller than 0.2, and the second larger than 0.2 [*Neugebauer*, 2006]. $B_n/|\mathbf{B}|$ was -0.0077 and 0.028 for $|\mathbf{B}|$ earthward and sunward of the discontinuity, respectively. $\Delta B/|\mathbf{B}|$ was 0.32 and 0.46 for $|\mathbf{B}|$ earthward and sunward of the discontinuity, respectively. Since $B_n/|\mathbf{B}|$ is small (<0.2) and $\Delta B/|\mathbf{B}|$ is large (>0.2), we conclude that this discontinuity is indeed a tangential discontinuity.

Table 1. Spacecraft Positions at 1250 UT[a]

Spacecraft	X_{GSM} (R_E)	Y_{GSM} (R_E)	Z_{GSM} (R_E)
Wind	263.9	16.6	21.6
ACE	229.4	−28.3	24.2
DSP/TC1	9.9	−4.0	−5.8
THEMIS A	6.3	7.7	−4.1
Cluster 1	−4.9	−19.3	−4.0
Cluster 2	−6.2	−19.1	−3.6
Cluster 3	−5.3	−18.8	−3.5

[a]Times are 1150 UT for Wind and 1140 UT for ACE.

[12] We also estimated uncertainties in the orientations of the eigenvectors in the way described by *Sonnerup and Scheible* [1998, section 8.3.1]. The angular uncertainties were $\varphi_{31} = 0.90°$ and $\varphi_{32} = 2.3°$, where φ_{31} (φ_{32}) is the expected angular uncertainty of eigenvector $\mathbf{x}_3$ for rotation toward or away from eigenvector $\mathbf{x}_1$ ($\mathbf{x}_2$). The eigenvectors $\mathbf{x}_1$, $\mathbf{x}_2$, and $\mathbf{x}_3$ correspond to maximum, intermediate, and minimum variances, respectively.

[13] MVA applied to the ACE data gave a normal with a ratio of the intermediate-to-minimum eigenvalues of 19.9. The normal direction was $\phi = 177°$ and $\theta = -19°$. B_n was 0.73 ± 0.29 nT. $B_n/|\mathbf{B}|$ was small (0.077 and 0.13) and $\Delta B/|\mathbf{B}|$ was large (0.38 and 0.62), consistent with a tangential discontinuity. φ_{31} and φ_{32} were 0.73° and 3.2°, respectively.

[14] The timing analysis [*Russell et al.*, 1983; *Harvey*, 1998], with the use of Wind, ACE, and DSP/TC1 (see section 3.2 for DSP/TC1 observations), gave a normal and its speed (V_n) in two dimensions: ϕ = 174° and V_n = 410 km/s with the θ = 0° assumption. If we assume zero normal flow across a discontinuity (i.e., zero normal component of solar wind velocity ($\mathbf{v}_{SW}$) in the frame of a discontinuity (v'_{nSW}), a normal and its speed can be calculated in three dimensions. When we used $\mathbf{v}_{SW}$ = (−440, 30, −10) km/s obtained from the Wind observations, ϕ and θ were calculated to be 179° and −36°, respectively, and V_n was 363 km/s. A small discrepancy between v_n estimated from MVA and V_n from the 3-D timing analysis is probably due to an effect of the slowing down of the solar wind before its arrival at DSP/TC1, since DSP/TC1 was in the magnetosheath when the discontinuity arrived. This effect underestimates V_n in the analysis.

[15] It should be noted that the observed width of the discontinuity for this event was about 7.5 R_E. For comparison, the width of the discontinuity studied by *Maynard et al.* [2008] was about 5 R_E. Although the width of the structure that we analyze is large, solar wind plasma and IMF conditions on either side of it are consistent with those expected mathematically for an infinitely thin discontinuity. Therefore, we can determine the normal from MVA and CP with the data on both sides of the discontinuity.

[16] The above shown results of the estimates are summarized in Table 2. The "Window" column shows intervals selected for the estimates; for calculations of CP, two windows are selected to obtain upstream and downstream values, which are averaged over the selected intervals.

3.2. Observations in the Magnetosheath

[17] Figure 3 presents observations in the magnetosheath by DSP/TC1, THEMIS A and Cluster from top down. TC1 observed a B_y increase, a B_z increase, and a $|B|$ decrease between 1246:05 and 1247:05 UT, as indicated by black and red dashed lines. The profile is similar to that of the discontinuity observed by Wind and ACE. It is reasonable to conclude that the **B** changes at TC1 are associated with the discontinuity which was transmitted through the bow shock into the magnetosheath. The duration of the B changes was 1 min. TC1 saw a small structure ∼1 min before it observed the leading edge of the discontinuity, as indicated by a red dotted line; B_y is smaller and $|B|$ is larger inside the structure than in the surrounding regions. The **B** changes indicate that the structure is generated by the inward motion of the bow shock caused by the arrival of the discontinuity. We think that the front of the structure is the fast forward shock generated at the bow shock. About 1.5 min after TC1 observed the trailing edge of the discontinuity, it crossed the bow shock into the interplanetary space, as indicated by a light blue dashed-dotted line. This indicates that the bow shock was moving antisunward.

[18] THEMIS A observed sudden changes in B_y, B_z, and $|B|$ between 1249:35 and 1250:40 UT. Since the profile is similar to that of the discontinuity in the solar wind, we conclude that the changes are the transmitted discontinuity that is seen by TC1. The discontinuity spent 65 s to pass by the THEMIS A location. A magnetic field change at 1247 UT was due to the magnetopause crossing. The ion energy-time diagram (third panel) clearly indicates the crossing; the magnetosheath plasma appeared after 1247 UT.

[19] Cluster 1, 2, and 3 saw magnetic field variations from 1248 to 1252 UT, which are similar to those observed by TC1. B_y increased and $|B|$ decreased at 1250–1251 UT about 2 min after B_y decreased and $|B|$ increased. The variations indicate the transmitted discontinuity following the compressed region generated by inward motion of the bow shock caused by the arrival of the discontinuity. The transmitted discontinuity took 40–45 s to pass by the spacecraft location; it is shorter than at the locations of TC1 and THEMIS A.

[20] Figure 4 shows magnetic field and ion data obtained by THEMIS A and Cluster 1. Ion density increased by a factor of ∼2 at both spacecraft near 1250 UT at the arrival of the leading edge of the transmitted discontinuity. The X component of ion velocity, on the other hand, increased at the fast forward shock and remained almost constant at the discontinuity. The increase can be seen ∼20 s later than the **B** change. This is probably because the fast shock has a "shock foot" region ahead of it.

3.3. Normal Direction of the Fast Forward Shock and the Discontinuity

[21] We estimate the normal direction and speed of the discontinuity in the magnetosheath and the fast forward shock generated at the bow shock and propagating in the magnetosheath. We use MVA and CP of the magnetic field for the discontinuity, and MVA and the magnetic coplanarity (MC) method [*Colburn and Sonett*, 1966] for the fast forward shock.

3.3.1. Fast Forward Shock

[22] We apply MVA and the MC method to magnetic field data obtained by TC1 and Cluster 1, 2, and 3 shown in Figure 3. The normal vector is expressed in the MC method as:

$$\mathbf{n} = \pm \frac{(\mathbf{B}_1 - \mathbf{B}_2) \times (\mathbf{B}_1 \times \mathbf{B}_2)}{|(\mathbf{B}_1 - \mathbf{B}_2) \times (\mathbf{B}_1 \times \mathbf{B}_2)|},$$

where the subscripts 1 and 2 of **B** refer to the magnetic field ahead of and behind the shock, respectively. The results are summarized in Table 2. The "Window" column shows intervals selected for the estimates; for calculations of MC, upstream and downstream values are averaged over the selected intervals. The "Ratio" column lists the ratio of intermediate to minimum eigenvalues derived from MVA. THEMIS A did not see the forward shock, because it was in the magnetosphere when the shock arrived.

[23] All MVA estimates gave similar results for ϕ (∼180°) and modest differences in θ (2.1°–34°). The bottom row is the results based on the timing analysis using Cluster 1, 2, and 3; we chose the times indicated by magenta dotted lines in the fourth, fifth, and sixth panels in Figure 3. The estimates gave ϕ = −147°, which was about 30° different from the other estimates. We believe that the differences arise from uncertainties for determination of the onset of $|B|$ increases and B_y decreases. We conclude that the front of the fast forward shock is almost aligned with the Sun-Earth line.

Table 2. Estimates of the Propagation Normal and Speed: the Density-Increase Event[a]

Spacecraft	Method	Window (UT)	ϕ (deg)	θ (deg)	V_n (km/s)	Ratio	$\Delta\varphi_{31}$ (deg), $\Delta\varphi_{32}$ (deg)	B_n (nT)	$B_n/\lvert\mathbf{B}\rvert$	$\Delta\lvert B\rvert/\lvert B\rvert$
				Solar Wind Discontinuity						
Wind	MVA	1140:00–1145:00	178	−20		8.0	0.90, 2.3	−0.092 ± 0.29	−0.0077, 0.028	0.32, 0.46
	CP	1139:20–1141:20, 1144:00–1146:00	−179	−26						
ACE	MVA	1147:30–1152:30	177	−19		19.9	0.73, 3.2	0.73 ± 0.29	0.077, 0.13	0.38, 0.62
	CP	1147:00–1149:00, 1151:00–1153:00	174	−28						
Wind, ACE, TC1	Timing (2-D)		174		410					
Wind, ACE, TC1	Timing (3-D)	$v'_{nSW} = 0$ assumption	177	−25	393					
				Fast Forward Shock in the Magnetosheath						
TC1	MVA	1244:00–1246:00	180	28		2.2	4.7, 12.8			
	MC	1244:30–1245:10, 1245:20–1246:00	179	29						
Cluster 1	MVA	1247:00–1250:00	150	7.8		5.7	2.0, 4.5			
	MC	1247:20–1248:00, 1249:20–1250:00	179	14						
Cluster 2	MVA	1247:00–1250:00	178	2.1		10.9	1.4, 2.9			
	MC	1247:40–1248:20, 1249:40–125020	−174	34						
Cluster 3	MVA	1247:00–1250:00	176	29		2.6	1.8, 8.7			
	MC	1247:20–1248:00, 1249:20–1250:00	−176	34						
Cluster 1, 2, and 3	Timing (2-D)		−147		287					
				Discontinuity in the Magnetosheath						
TC1	MVA	1245:30–1247:30	170	21		16	1.4, 2.8	2.0 ± 1.3	0.043, 0.088	0.42, 0.71
	CP	1245:20–1246:00, 1247:20–1248:00	168	13						
Cluster 1	MVA	1249:30–1252:30	146	−3.9		17	1.0, 2.3	−1.4 ± 0.65	−0.053, −0.054	0.26, 0.35
	CP	1249:20–1250:00, 1251:20–1252:00	147	−0.14						
Cluster 2	MVA	1250:00–1253:00	144	−4.5		9.8	1.2, 3.1	−1.4 ± 0.88	−0.046, −0.054	0.27, 0.36
	CP	1249:40–1250:20, 1251:40–1252:20	141	3.6						
Cluster 3	MVA	1249:30–1252:30	143	−0.84		8.9	1.1, 3.3	−1.2 ± 0.93	−0.021, −0.049	0.32, 0.47
	CP	1249:20–1250:00, 1251:30–1252:10	142	4.3						
Cluster 1, 2, and 3	Timing (2-D)		140		188					
Cluster 1, 2, and 3	Timing (2-D)	$v'_{nSW} = 0$ assumption	138	−4.5	176					
THEMIS A	MVA	1248:00–1252:00	−154	18		29	0.66, 1.3	1.4 ± 0.89	−0.0050, −0.032	0.18, 0.22
	CP	1248:30–1249:00, 1251:30–1252:10	−152	17						

[a]Notes: ϕ, longitude in GSM coordinates; θ, latitude in GSM coordinates; Ratio, ratio of intermediate to minimum eigenvalues; v'_{nSW}, normal component of solar wind velocity in the frame of the discontinuity; V_n, normal velocity of the discontinuity or the fast shock.

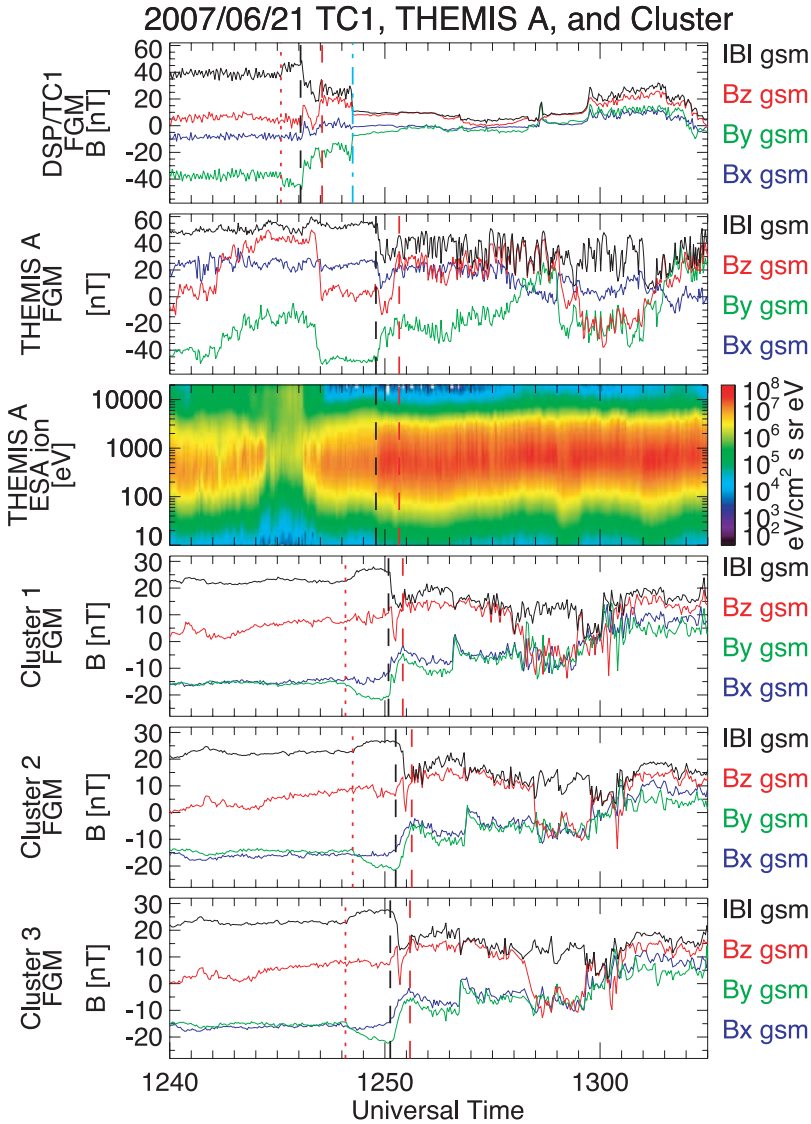

Figure 3. Observations by DSP/TC1 in the magnetosheath near noon, THEMIS A around the magnetopause on the duskside, and Cluster in the dawnside magnetosheath between 1240 UT and 1305 UT. Black and red dashed lines indicate the leading and trailing edges of the discontinuity. A light blue dashed-dotted line indicates the bow shock crossing. Magenta dotted lines show the arrival of the forward fast shock.

3.3.2. Discontinuity in the Magnetosheath

[24] We apply MVA and CP to magnetic field data obtained by TC1, THEMIS A, and Cluster 1, 2, and 3. The results are summarized in Table 2; the format is the same as the solar wind discontinuity portion of Table 2. The normal direction was $\phi \sim 170°$ at TC1, $\phi \sim 145°$ at Cluster, and $\phi \sim -153°$ at THEMIS A. The 2-D timing analysis with Cluster 1, 2, and 3 gave $\phi = 140°$ which is consistent with the other estimates. The results clearly indicate that the transmitted discontinuity is deformed into a concave shape, tilted toward dusk (dawn) on the dawnside (duskside).

[25] All MVA estimates gave high eigenvalue ratios, small $|B_n|$, small $B_n/|\mathbf{B}|$ (<0.1), and large $\Delta B/|\mathbf{B}|$ (>0.18), suggesting that the discontinuity remains a tangential discontinuity in the magnetosheath. In fact, the estimated normal is close to that estimated from CP. Furthermore, the timing analysis at Cluster with the zero v'_{nSW} assumption gave similar results.

4. Density Decrease Event

[26] A discontinuity, across which the density decreases, arrived at Wind at 0909:50 UT and at ACE at 0916:40 UT. It reached the bow shock around 1010 UT, when DSP/TC1, THEMIS, and Cluster were located in the magnetosheath near noon, on the duskside and on the dawnside, respectively. Positions of the spacecraft are summarized in Figure 5 and Table 3.

4.1. Solar Wind Observations

[27] Figure 6 shows Wind and ACE observations at 0900–0925 UT. The magnetic field changed at Wind

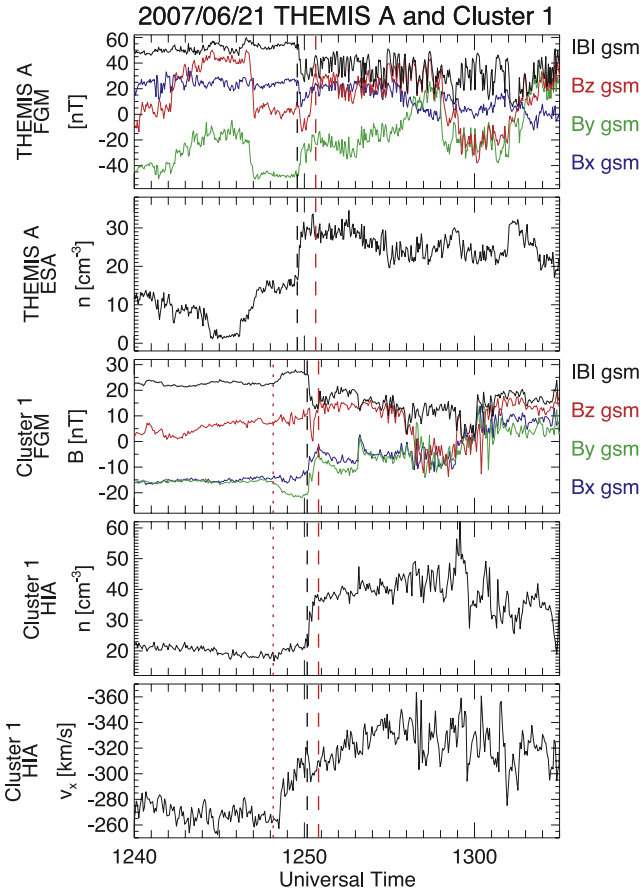

Figure 4. Magnetic field and ion data obtained by THEMIS A and Cluster 1 at 1240–1305 UT. Dashed and dotted lines are drawn in the same way as in Figure 3.

between 0909:50 and 0912:20 UT; both times are indicated by black and red dashed lines, respectively. B_y decreased from −5 to −8 nT and B_z increased from −6 to 10 nT. The field strength increased from 6 to 12 nT. The density decreased ∼40% of its original value simultaneously, while the X component of velocity remained almost constant, and therefore the dynamic pressure decreased. The thermal plasma pressure decreased and the magnetic pressure increased across the discontinuity.

[28] The magnetic field measured at ACE around 0918 UT shows a similar profile to that at Wind. B_y decreased from −5 to −9 nT and B_z increased from −6 to 8 nT. The field strength increased from 8 to 11 nT.

[29] We discuss the nature of the discontinuity in the same way as in section 3.1. MVA performed with the Wind data over the interval of 0909:00–0913:00 UT gave a normal with a ratio of the intermediate-to-minimum eigenvalues of 5.8. The normal was $\phi = -171°$ and $\theta = 11°$. B_n was 3.86 ± 0.37 nT. v_n was 409 km/s, being nearly constant, and its standard deviation was 3.2 km/s. p was 0.058 nPa and its standard deviation was 0.0068 nPa. $B_n/|\mathbf{B}|$ was 0.52 and 0.30 for $|\mathbf{B}|$ earthward and sunward of the discontinuity. $\Delta B/|\mathbf{B}|$ was 0.61 and 0.38 for $|\mathbf{B}|$ earthward and sunward of the discontinuity. The angular uncertainties were $\varphi_{31} = 0.48°$ and $\varphi_{32} = 3.2°$. MVA applied to the ACE data gave a normal with a ratio of the intermediate-to-minimum eigenvalues of 11.0. The normal was $\phi = 174°$ and $\theta = 6.2°$. B_n was 1.43 ± 0.65 nT. $B_n/|\mathbf{B}|$ was 0.17 and 0.14, and $\Delta B/|\mathbf{B}|$ was 0.32 and 0.24. φ_{31} and φ_{32} were 0.75° and 5.1°, respectively. The timing analysis with the use of Wind, ACE, and DSP/TC1 (see section 4.2 for DSP/TC1 observations), gave a normal and V_n in two dimensions: $\phi = 170°$ and $V_n = 395$ km/s with the $\theta = 0°$ assumption. Under the $v'_{nSW} = 0$ assumption with $\mathbf{v}_{SW} = (-420, 0, -20)$ km/s from the Wind observations, ϕ and θ were calculated to be 174° and −34°, respectively, and V_n was 358 km/s. We used the arrival times of the leading edge of the discontinuity at Wind, ACE, and DSP/TC1 for the timing analysis.

[30] The above shown results of the estimates are summarized in Table 4 in the same format as in Table 2. The calculations with the Wind data show that v_n was constant on both sides of the discontinuity, while p was not completely constant across the discontinuity. $\Delta B/|\mathbf{B}|$ was large, while $B_n/|\mathbf{B}|$ was not small. The discontinuity does not completely satisfy requirements for a tangential discontinuity. The spatial width of this structure was about 9 R_E. This structure, followed by a region with low plasma beta (<0.2), seems to be the front of the magnetic cloud [e.g., *Lepping et al.*, 1996]. The nonconstant p and nonzero B_n may be related to an expansion of the magnetic cloud [e.g., *Klein and Burlaga*, 1982] and/or a complex layer in front of the magnetic cloud body (i.e., in the magnetic cloud boundary layer) [e.g., *Wei et al.*, 2006; *Farrugia et al.*, 2008]. Since this study focuses on a sudden decrease in density and a sudden increase in $|\mathbf{B}|$, we call the structure a (density-decrease) discontinuity in this study. Since solar wind and

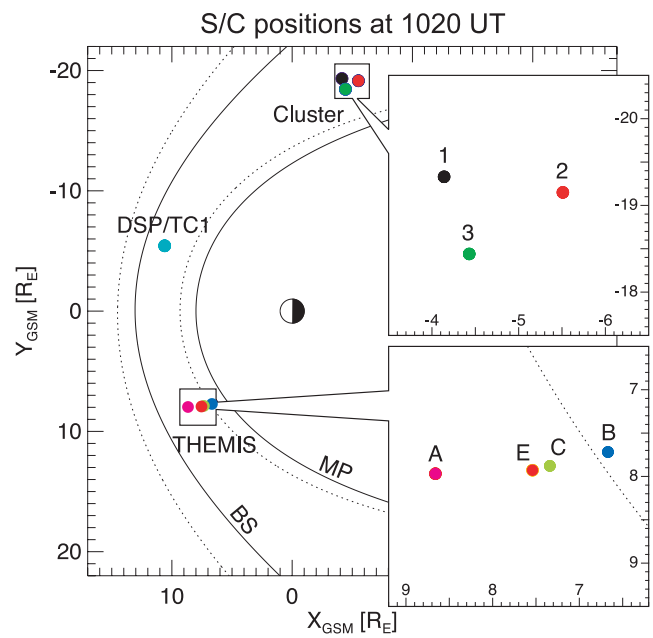

Figure 5. Spacecraft positions at 1020 UT. BS and MP denote the bow shock and the magnetopause, respectively. The locations of BS and MP are based on models by *Peredo et al.* [1995] and *Shue et al.* [1998]. Solid and dotted lines represent the locations before and after the arrival of the discontinuity; we choose input parameters for the models so that the model magnetopause locations can reproduce the THEMIS B magnetopause crossing.

Table 3. Spacecraft Positions at 1020 UT[a]

Spacecraft	X_{GSM} (R_E)	Y_{GSM} (R_E)	Z_{GSM} (R_E)
Wind	263.9	16.5	−4.7
ACE	229.4	−28.8	23.6
DSP/TC1	10.6	−5.4	−5.5
THEMIS A	8.5	8.0	−4.8
THEMIS B	6.5	7.7	−4.3
THEMIS C	7.2	7.8	−4.5
THEMIS E	7.4	7.9	−4.6
Cluster 1	−4.2	−19.3	−2.5
Cluster 2	−5.5	−19.2	−2.1
Cluster 3	−4.5	−18.5	−2.0

[a]Times are 0910 UT for Wind and 0920 UT for ACE.

IMF conditions on either side of the discontinuity are similar to those expected mathematically for an infinitely thin discontinuity, it is reasonable to determine the normal from MVA and CP with the data on both sides of the discontinuity. We conclude that the discontinuity normal is inclined 0°–10° toward dusk and ∼10° toward north.

[31] Black dotted lines shown ahead of the discontinuity indicate small changes of the magnetic field, which are used as a reference of solar wind propagation.

4.2. Observations in the Magnetosheath

[32] Figure 7 shows observations in the magnetosheath by DSP/TC1; THEMIS A, E, C, and B; and Cluster 1, 3, and 2 from the top. TC1 observed a B_y decrease, a B_z increase, and a $|B|$ increase starting at 1013:30 UT. It crossed the bow shock at 1016:20 UT indicated by a light blue dotted line. The change in **B** ended around 1018 UT. The profile is consistent with that observed by Wind and ACE in the solar wind, except that TC1 crossed the bow shock. TC1 observed small changes in B_y and B_z at 1009:40 UT, as indicated by a black dotted line; the changes are similar to those observed by Wind and ACE ahead of the discontinuity. We believe that the **B** changes between the black and red dashed lines are due to the arrival of the discontinuity.

[33] THEMIS A, E, and C crossed the bow shock before they observed **B** changes: a B_z increase and a $|B|$ increase. The changes are similar to those seen in the discontinuity observed in the solar wind by Wind and ACE, except that an overshoot of $|B|$ appears at the trailing edge (red dashed line) at THEMIS C and E. In addition, before crossing the bow shock, THEMIS observed small **B** changes (black dotted lines) similar to those found ahead of the solar wind discontinuity. It is reasonable to conclude that the **B** changes are due to the arrival of the discontinuity transmitted through the bow shock. Differences among THEMIS A, E, and C are the durations of the whole discontinuity (between black and red dashed lines) and the reversal times of B_z near the trailing edge (red dashed lines). B_z at THEMIS A, E, and C reversed at ∼1016–∼1021 UT, ∼1020–∼1024 UT, and ∼1024–∼1025 UT, respectively. The duration (reversal time) becomes longer (shorter) for spacecraft further away from the bow shock.

[34] THEMIS B observed a small B_y decrease and B_z increase which are similar to the variations ahead of the discontinuity. It experienced a big jump in B_z at 1019:00 UT followed by undisturbed magnetic field, as indicated by a pink dotted-dashed line. The jump is due to the magnetopause crossing; an ion energy-time diagram shows magnetospheric energetic ions and no magnetosheath plasma (not shown here). THEMIS B crossed the magnetopause at 1024:20 UT back into the magnetosheath, as indicted by the second pink dotted-dashed line. THEMIS B did not observe the discontinuity owing to its transient excursion into the magnetosphere.

[35] Cluster 1, 2, and 3 observed a similar B_z profile to that THEMIS A, E, and C observed. As seen in THEMIS data, the discontinuity durations (between black and red dashed lines) and the B_z reversal times (∼1017–1024 UT for Cluster 1 and ∼1023–∼1025 UT for Cluster 3 and 2) become longer and shorter, respectively, for a spacecraft located further away from the bow shock. An overshoot of $|B|$ is seen near the trailing edge (red dashed line) at all of the Cluster spacecraft.

[36] Figure 8 presents magnetic field and ion moment data from THEMIS. Density decreased gradually in the discontinuity at all spacecraft. It started to decrease before the leading edge of the discontinuity arrived. Figure 9 shows magnetic field, ion density, and ion velocity data from Cluster 1 and 3. Similar profiles of density and velocity are seen in the Cluster data. We suggest that the earlier density decrease is associated with the rarefaction waves generated at the bow shock through the interaction

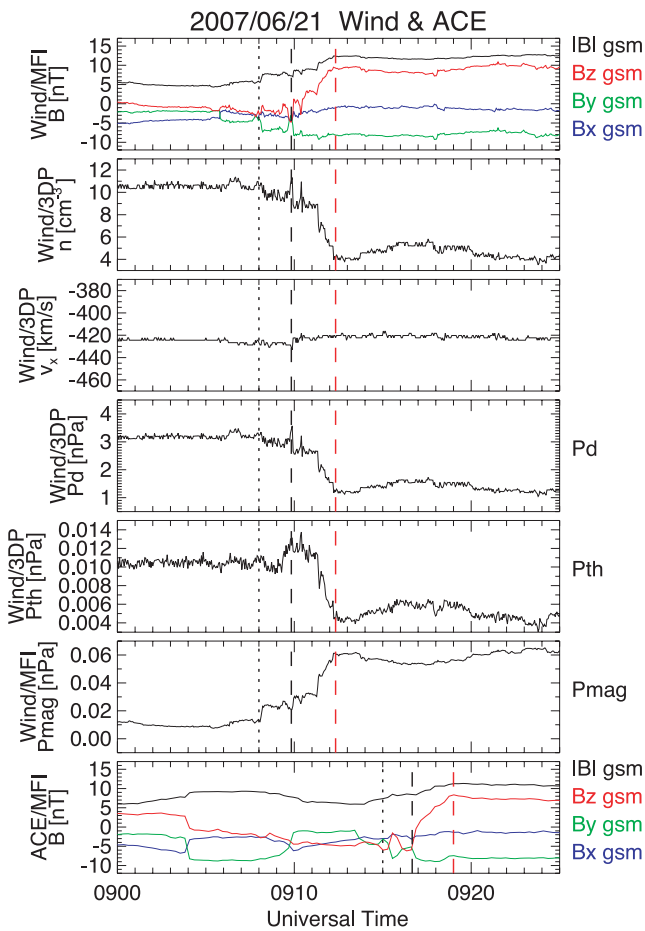

Figure 6. Solar wind observations by Wind and ACE between 0900 UT and 0925 UT. Black and red dashed lines indicate the leading and trailing edges of the discontinuity. Black dotted lines indicate a small **B** change ahead of the discontinuity.

Table 4. Estimates of the Propagation Normal and Speed: The Density-Decrease Event[a]

Spacecraft	Method	Window (UT)	ϕ (deg)	θ (deg)	V_n (km/s)	Ratio	$\Delta\varphi_{31}$ (deg), $\Delta\varphi_{32}$ (deg)	B_n (nT)	$B_n/\|B\|$	$\Delta\|B\|/\|B\|$
Solar Sind Discontinuity										
Wind	MVA	0909:00–0913:00	−171	11		5.8	0.48, 3.2	3.86±0.37	0.52, 0.30	0.61, 0.38
	CP	0908:30–0909:30, 0913:00–0914:00	158	13						
ACE	MVA	0913:00–0920:00	174	6.2		11.0	0.75, 5.1	1.43±0.65	0.17, 0.14	0.32, 0.24
	CP	0915:30–0916:30, 0919:30–0920:30	165	5.5						
Wind, ACE, TC1	Timing (2-D)		170		395					
Wind, ACE, TC1	Timing (3-D)	$v'_{nSW} = 0$ assumption	174	−34	358					
Discontinuity in the Magnetosheath: Estimates Based on MVA and CP										
THEMIS E	MVA	1010:00–1025:00	−141	17		13	0.37, 1.0	5.1±0.43	0.77, 0.14	8.0, 0.89
	CP	1010:00–1025:00	−156	17						
THEMIS C	MVA	1010:00–1026:00	−137	9.1		4.0	0.86, 2.2	7.4±1.0	0.80, 0.14	7.6, 0.88
	CP	1010:00–1026:00	−154	16						
Cluster 1	MVA	1010:00–1025:00	114	6.7		7.4	0.72, 1.7	−4.4±0.46	−0.74, −0.17	5.0, 0.83
	CP	1013:00–1016:00, 1025:00–1028:00	132	7.7						
Cluster 3	MVA	1010:00–1025:00	124	13		3.2	0.69, 3.1	−1.7±0.89	−0.25, 0.013	1.0, 0.50
	CP	1014:00–1017:00, 1026:00–1029:00	129	5.9						
Cluster 2	MVA	1011:00–1026:00	144	9.7		2.8	0.53, 3.7	4.2±0.94	0.14, 0.15	1.2, 0.54
	CP	1014:30–1017:30, 1026:00–1029:00	128	6.8						
Discontinuity in the Magnetosheath: Estimates Based on the Timing Analysis										
THEMIS A, C, and E										
Leading edge			−163		93					
Trailing edge			−116		21					
Cluster 1, 2, and 3										
Leading edge			112		147					
Trailing edge			130		108					

[a]Notes: ϕ, longitude in GSM coordinates; θ, latitude in GSM coordinates; Ratio, ratio of intermediate to minimum eigenvalues; v'_{nSW}, normal component of solar wind velocity in the frame of the discontinuity; V_n, normal velocity of the discontinuity.

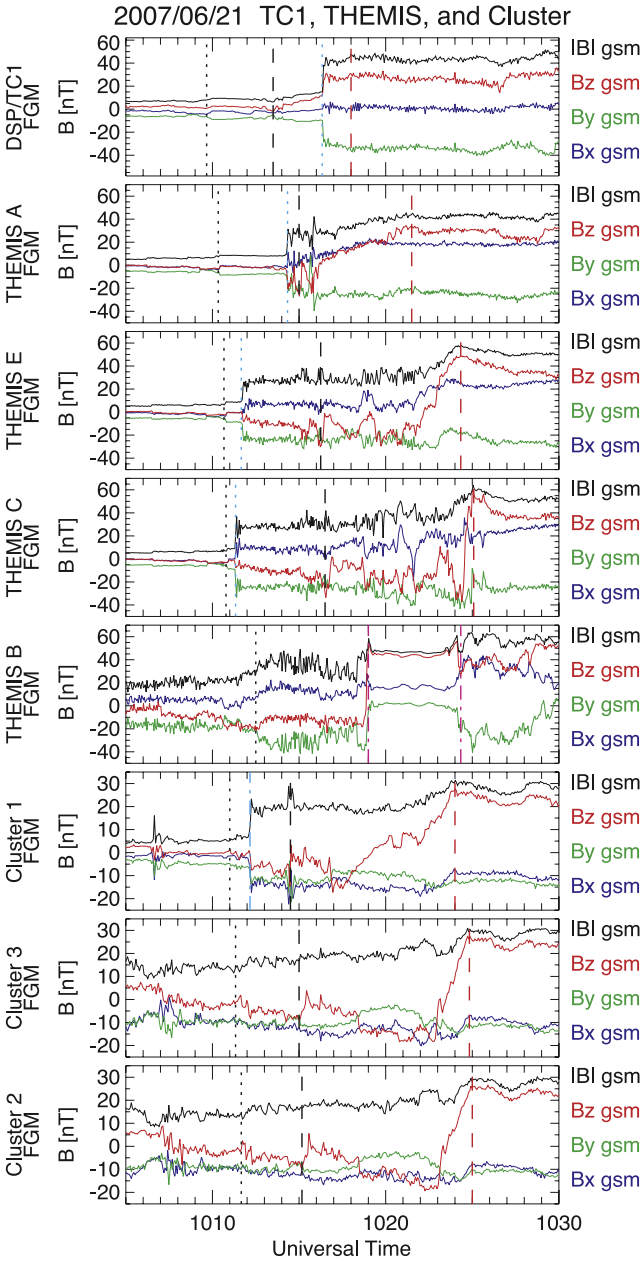

Figure 7. Magnetic field variations observed by TC1, THEMIS A, E, C, and B, and Cluster 1, 3, and 2 from 1005 UT to 1030 UT from top down. Black and red dashed lines indicate the leading and trailing edges of the discontinuity. Black dotted lines indicate a small **B** change ahead of the discontinuity. Light blue dashed-dotted lines are drawn at the bow shock crossing.

between the discontinuity and the bow shock, as theoretically proposed by *Völk and Auer* [1974].

[37] The X component of plasma flow and its magnitude decreased after the leading edge arrived, being slower inside the discontinuity than in the surrounding regions. We think that the slowing down is key to explain the broadening of the discontinuity. We discuss it in more detail in section 6.

4.3. Normal Direction of the Discontinuity

[38] We estimate the normal direction and speed of the discontinuity in the magnetosheath. We apply MVA to magnetic field data obtained by THEMIS E and C and Cluster 1, 2, and 3 shown in Figure 7. The results are summarized in Table 4; the format is the same as Table 2. The normal direction was $\phi = -137°$ at THEMIS C, $\phi = -141°$ at THEMIS E, $\phi = 114°$ at Cluster 1, $\phi = 144°$ at Cluster 2, and $\phi = 124°$ at Cluster 3 and $\theta \sim 10°$ at both THEMIS and Cluster. The results clearly indicate that the

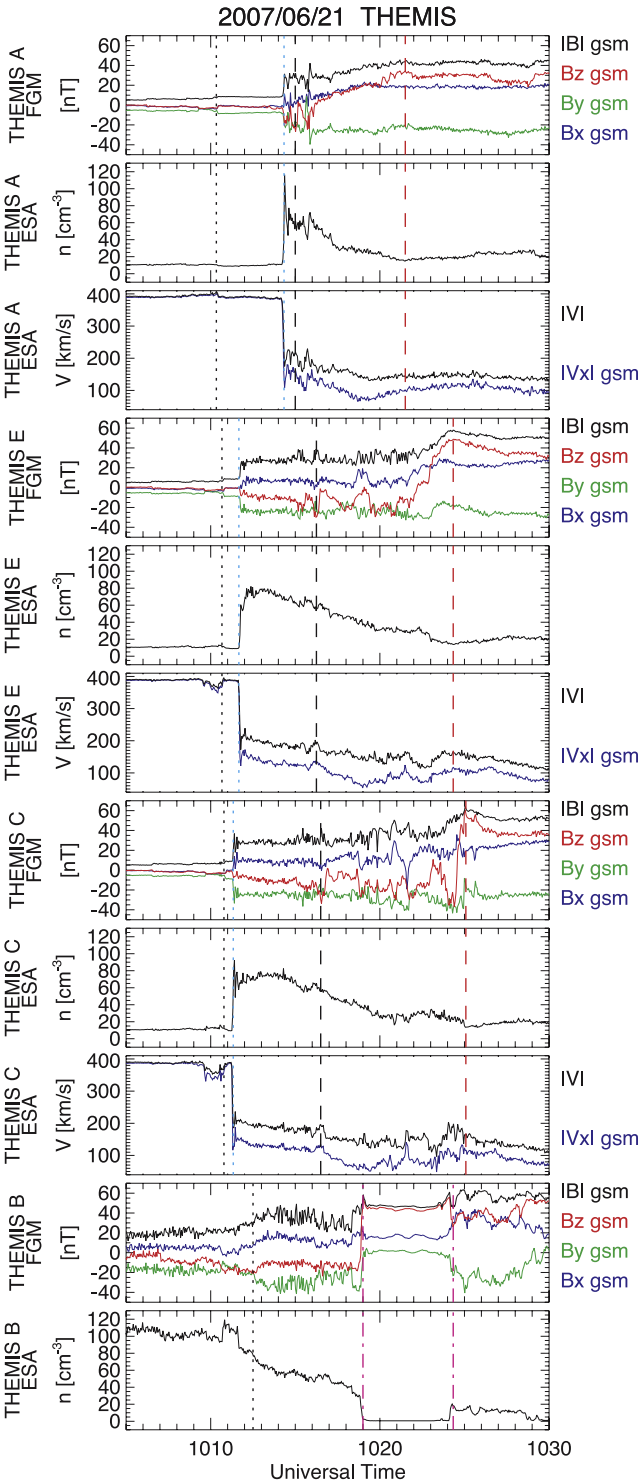

Figure 8. Magnetic field and ion data from THEMIS at 1005–1030 UT. Dashed and dotted lines are drawn in the same way as in Figure 7.

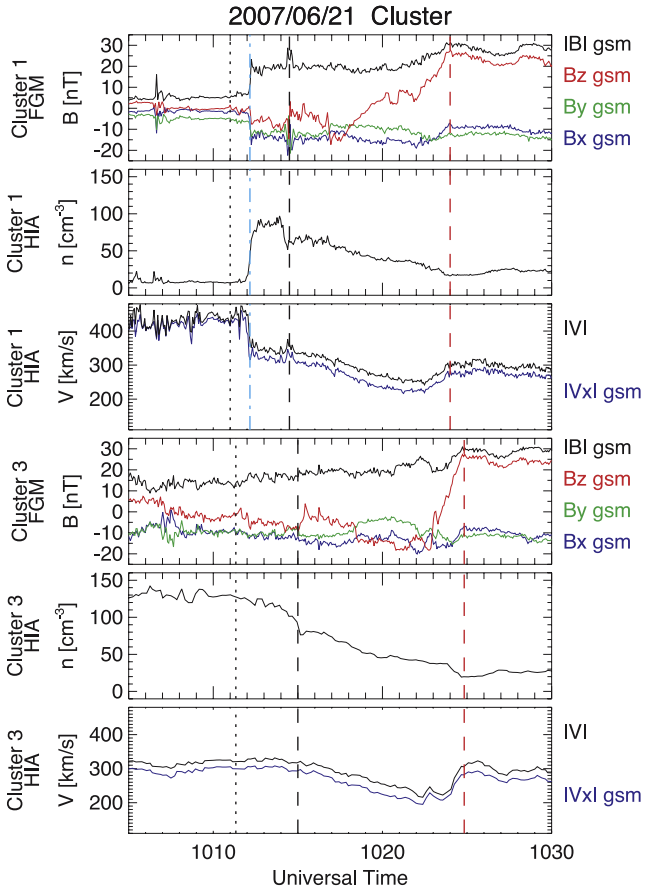

Figure 9. Magnetic field and ion data from Cluster at 1005–1030 UT. Dashed and dotted lines are drawn in the same way as in Figure 7.

transmitted discontinuity is deformed into a concave shape, tilted toward dusk (dawn) on the dawnside (duskside). Table 4 summarizes the results including calculations of CP. Although a normal derived from CP was similar to the MVA results, large B_n upstream (in the earthward side) of the discontinuity did not satisfy requirements for a tangential discontinuity. It is difficult to classify this discontinuity into a category, since this discontinuity has expanded and its internal structure evolved as it propagates in the magnetosheath (see next paragraph and Discussion),

[39] Next, we conducted the timing analysis in 2-D with the use of THEMIS data. We estimated the normal direction and speed of the leading edge (black dashed lines in Figure 7) and the trailing edge (red dashed lines) of the discontinuity. Table 4 summarizes the results. The bottom two rows list the same estimates based on Cluster data. In general, both the leading and trailing edges are inclined toward dusk on the dawnside and toward dawn on the duskside. The speed of the trailing edge is slower than the leading edge.

5. Theoretical Analysis

5.1. Calculations Based on Rankine-Hugoniot Equations

[40] The observations shown in sections 3 and 4 indicated differences in the duration of the discontinuity crossing among different spacecraft. This suggests the evolution of the spatial width of the discontinuity in the magnetosheath, because the solar wind speed is virtually unchanged between the locations of the spacecraft. We believe that the evolution is associated with variations of solar wind velocity downstream of the bow shock. The variations are most likely produced by the bow shock motion caused by an impingement of the discontinuity on the bow shock.

[41] In this section, we calculate the plasma velocity downstream of the bow shock, using upstream plasma properties and taking into account the motion of the bow shock. We use a simplified approach based on Rankine-Hugoniot (R-H) equations [cf. *Lepping and Argentiero*, 1971; *Baumjohann and Treumann*, 1996; *Petrinec and Russell*, 1997; *Kabin*, 2001] to qualitatively explain the observations.

[42] The R-H equations, under the assumption that the shock front is locally planar and the plasma is isotropic on both sides of the shock, are expressed as

$$\begin{aligned}
&[nv_n] = 0 \\
&mnv_n[v_n] + \left[p + \frac{B_t^2}{2\mu_0}\right] = 0 \\
&nv_n[\mathbf{v}_t] - \left[\frac{B_n}{\mu_0}\mathbf{B}_t\right] = 0 \\
&\left[v_n\left(\frac{1}{2}nmv^2 + \frac{\gamma}{\gamma-1}p + \frac{B_t^2}{\mu_0}\right) - \frac{B_n}{\mu_0}(\mathbf{v}_t\cdot\mathbf{B}_t)\right] = 0 \\
&[B_n\mathbf{v}_t - v_n\mathbf{B}_t] = 0 \\
&[B_n] = 0
\end{aligned} \quad , \qquad (1)$$

where n is density, m is mass, v is plasma speed, p is plasma thermal pressure, B is the magnetic field strength, μ_0 is the magnetic constant, $\mathbf{v}$ is velocity, and $\mathbf{B}$ is the magnetic field. The subscripts n and t denote the normal and tangential component of the corresponding vectors, respectively. The quantity $[A]$ is the jump of a variable A across the boundary. γ is the specific heats ratio, for which we choose a constant value of 5/3 on both sides of the bow shock.

[43] The discontinuities examined in the present study had the normals almost aligned with the Sun-Earth line; that is, the discontinuity front was perpendicular to the Sun-Earth line. v_n in the rest frame dominated plasma velocity. The normal component of the magnetic field across the discontinuities was small. Therefore, in the following calculations, we assume that upstream velocity ($\mathbf{v}_1$) is parallel to the Sun-Earth line ($v_1 = v_{x1}$) and that the upstream magnetic field ($\mathbf{B}_1$) is perpendicular to the Sun-Earth line ($B_1 = B_{y1}$). In the following descriptions, upstream and downstream quantities are denoted by the subscripts 1 and 2.

[44] When the bow shock normal is parallel to $\mathbf{v}_1$, B_n across the bow shock is zero. This condition applies to the interactions at the subsolar point. In this condition, the equation (1) can be rewritten as a second-order equation for the inverse of the ratio of downstream to upstream density ($\varepsilon = n_2/n_1$):

$$\frac{\gamma+1}{\gamma-1}\cdot M_A^2\left(\frac{1}{\varepsilon}\right)^2 - \left[M_A^2 + \frac{\gamma}{\gamma-1}(1+\beta)\right]\left(\frac{1}{\varepsilon}\right) + \frac{\gamma-2}{\gamma-1} = 0, \qquad (2)$$

where M_A is Alfvén Mach number ($M_A = v(mn\mu_0)^{1/2}/B$), and β is plasma beta ($\beta = 2\mu_0 p/B^2$). See *Wu et al.* [1993] for more details.

[45] When v_{n1} is not parallel to the bow shock normal, B_n is not zero across the bow shock. In this condition, equation (1) can be combined into the following third-order polynomial equation for ε:

$$\left(A_1^2 - \varepsilon\right)^2 \left[A_1^2 - \frac{2\varepsilon S_1^2}{\varepsilon + 1 - \gamma(\varepsilon - 1)}\right] - \varepsilon k_1^2 A_1^2 \cdot \left[\frac{2\varepsilon - \gamma(\varepsilon - 1)}{\varepsilon + 1 - \gamma(\varepsilon - 1)} A_1^2 - \varepsilon\right] = 0, \quad (3)$$

where A = $M_A\cos(\alpha)/\cos(\alpha\text{-}\theta)$, S = $M_A/M_s\cos(\alpha\text{-}\theta)$, and $k = \tan(\alpha\text{-}\theta)$. M_s is sonic Mach number ($M_s = v(\gamma p/mn)^{-1/2}$), α is the angle between **v** and the bow shock normal, and θ is the angle between **v** and **B**. The subscript 1 denotes quantities based on the upstream parameters. See *Petrinec and Russell* [1997] and *Kabin* [2001] for more details. We set $\theta = 90°$ because we are assuming the situations where $\mathbf{v}_1$ ($\mathbf{B}_1$) is parallel (perpendicular) to the Sun-Earth and therefore $\mathbf{v}_1$ is perpendicular to $\mathbf{B}_1$.

[46] Once ε is obtained from equation (1) or (2) with a set of upstream quantities, v_{n2} is determined from the first equation of equation (1) ($n_2/n_1 = v_{n1}/v_{n2} = \varepsilon$), and then v_{x2} and $|v|_2$ are obtained with the use of equation (1). When the bow shock motion is taken into account, v_n is replaced by $v_n - v_{BS}$ in calculations of M_A and M_s, where v_{BS} v_{BS} is the bow shock velocity. This means that the R-H equations are solved in the frame of the bow shock.

[47] In the following, we calculate $|v|_2$ and v_{x2} under upstream conditions similar to those obtained by Wind during the intervals examined in the present study (i.e., during the observations of the two discontinuities). For simplicity, we assume that upstream parameters are constant outside the discontinuities and that sharp gradients of the quantities inside the discontinuity are linear with time. v_1 is assumed to be constant on both sides of the discontinuities. We assume that the bow shock starts to move when the leading edge of the discontinuity hit the bow shock and its speed varies linearly with time up to a constant maximum value. *Wu et al.* [1993] found in their 1-D modeling that the bow shock, a tangential discontinuity, and a fast shock in the magnetosheath move with constant velocities after the interaction. We assume that the R-H conditions are satisfied in the frame of the bow shock even while the bow shock is moving (i.e., $v_{BS} \neq 0$).

[48] Figure 10 shows upstream quantities corresponding to the density-increase discontinuity examined in the present study, v_{BS}, and calculated $|v|_2$ and v_{x2}. We conducted the calculations with six different maximum values of earthward v_{BS}: 0, 30, 60, 90, 120, and 150 km/s, because the bow

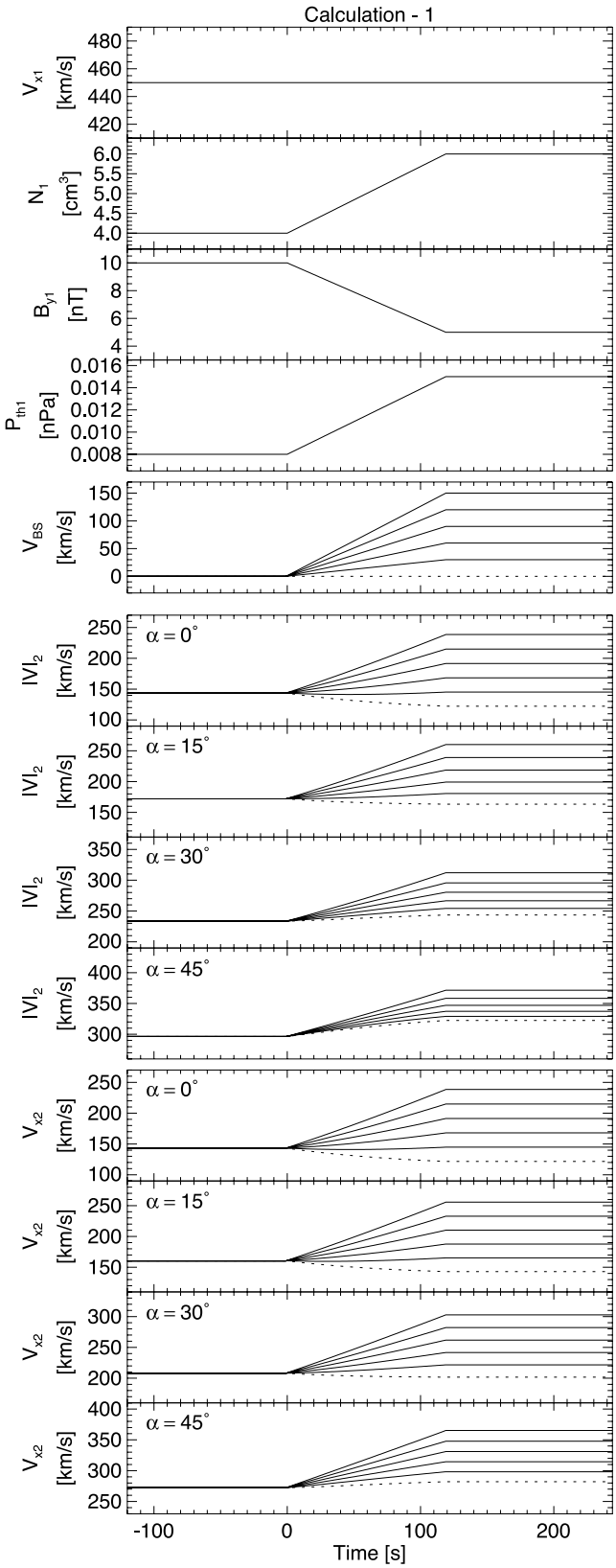

Figure 10. Calculations of the magnitude and X component of plasma velocity downstream of the bow shock ($|v|_2$ and v_{x2}) with the use of the Rankine-Hugoniot equations. The first through fourth panels show upstream quantities used in the calculations, which correspond to the density-increase discontinuity examined in this study. The fifth panel is the bow shock antisunward velocity that was taken into account; we choose six different values. The sixth through thirteenth panels show variations of the calculated $|v|_2$ and v_{x2}. The calculations were conducted with four different values of α, which is the angle between the upstream velocity vector and the bow shock normal.

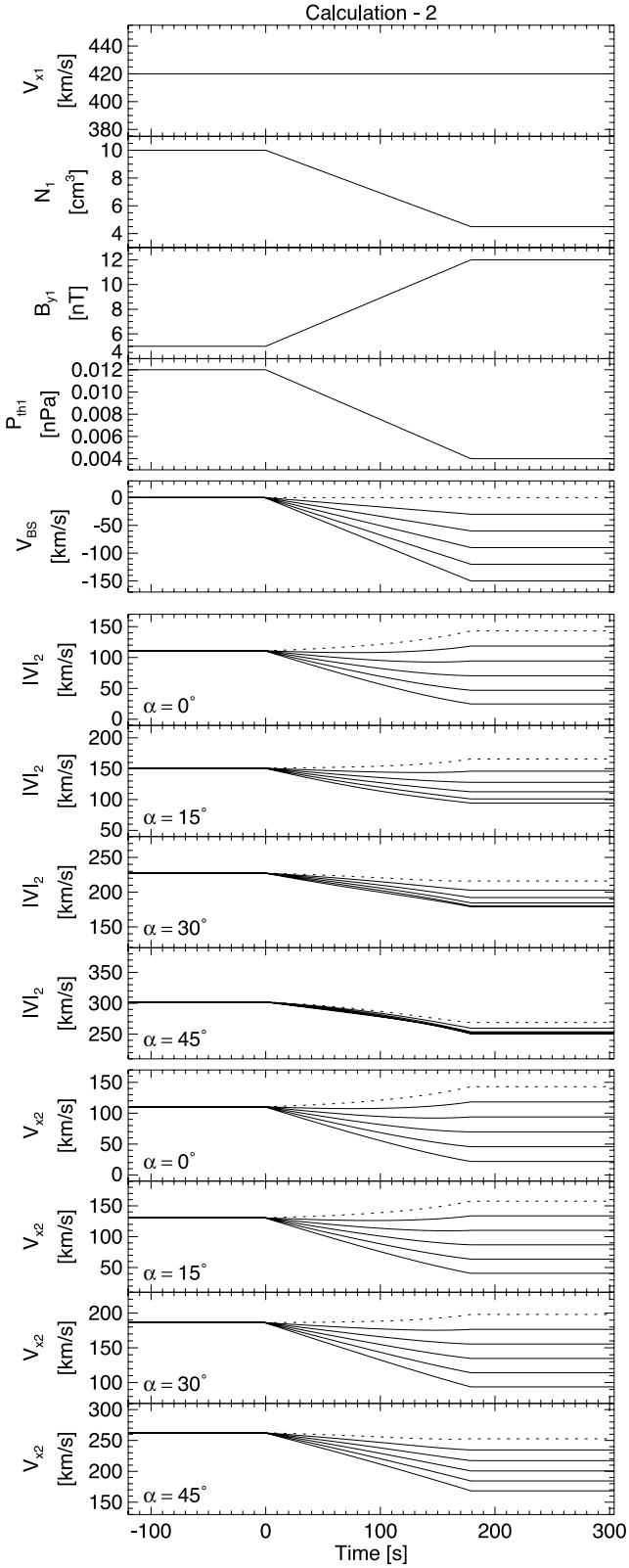

Figure 11. Calculations of the magnitude and X component of plasma velocity downstream of the bow shock ($|v|_2$ and v_{x2}) with the use of the Rankine-Hugoniot equations in the same format as Figure 10. The upstream quantities used here correspond to the density-decrease discontinuity examined in this study.

shock moves earthward when it is hit by a discontinuity accompanied by a density increase [*Völk and Auer*, 1974]. We also made the calculations with different values of α: 0, 15, 30, and 45°. The results for $\alpha = 0$ were derived from equation (2). The calculations show that, when $\alpha = 0°$, $|v|_2$ at the trailing edge of the discontinuity is slower than that at the leading edge if the bow shock stands still. On the other hand, $|v|_2$ at the trailing edge is faster than that at the leading edge when the bow shock moves earthward. $|v|_2$ inside the discontinuity is faster for plasma closer to the trailing edge (further away from the leading edge). These characteristics appear also for $|v|_2$ when $\alpha = 15°$ and for v_{x2} when $\alpha = 0°$, 15° and 30°. For the other cases shown in Figure 10, $|v|_2$ (v_{x2}) at the trailing edge is faster than that at the leading edge regardless of the bow shock motion. $|v|_2$ and v_{x2} at the trailing edge become faster as the bow shock earthward motion becomes faster. These results indicate that the bow shock earthward motion is responsible for the plasma speed faster near the trailing edge than near the leading edge. Such speed variations inside the discontinuity cause the discontinuity to be compressed as it propagates in the magnetosheath.

[49] Figure 11 plots the variables correspond to the density-decrease discontinuity in the same format as Figure 10. We choose six different maximum values for sunward v_{BS}: 0, 30, 60, 90, 120, and 150 km/s, because the bow shock moves sunward when it is hit by a discontinuity with a density decrease [*Völk and Auer*, 1974]. The calculations show that, when $\alpha = 0°$ and 15°, $|v|_2$ at the trailing edge is faster than that at the leading edge when the bow shock stands still. On the other hand, $|v|_2$ at the trailing edge is slower than that at the leading edge when the bow shock moves sunward; $|v|_2$ inside the discontinuity is slower for plasma close to the trailing edge (except for its speed assumed 30 km/s with $\alpha = 0°$). Similar results are seen for v_{x2} when $\alpha = 0°$, 15°, and 30°. For the other cases shown in Figure 11, $|v|_2$ (v_{x2}) at the trailing edge is slower than that at the leading edge regardless of the bow shock motion. $|v|_2$ and v_{x2} at the trailing edge become slower as the bow shock sunward motion becomes faster. These results indicate that the bow shock sunward motion is responsible for the plasma speed slower near the trailing edge than near the leading edge. Such speed variations inside the discontinuity cause the discontinuity to be expanded as it propagates in the magnetosheath.

5.2. MHD Modeling

[50] In this section we further analyze the deformation and evolution of the two discontinuities in the magnetosheath, using a numerical MHD simulation. The MHD model is mathematically based on the equations of ideal single-fluid magnetohydrodynamics. The equations are solved on a three-dimensional unstructured adaptive grid with over 4 million cells and the smallest cell size of 0.156 Earth radii. The spatial resolution in the solar wind area proper (upstream of the bow shock) is $4 \times 0.156\ R_E$; the magnetosheath for the most part had a resolution of $2 \times 0.156\ R_E$. The grid structure is not changed during the simulation. The computed solution was saved every 20 s. The technical and numerical details of this simulation code are described by *Powell et al.* [1999] and *Tóth et al.* [2005]. Examples of the model application to the terrestrial magne-

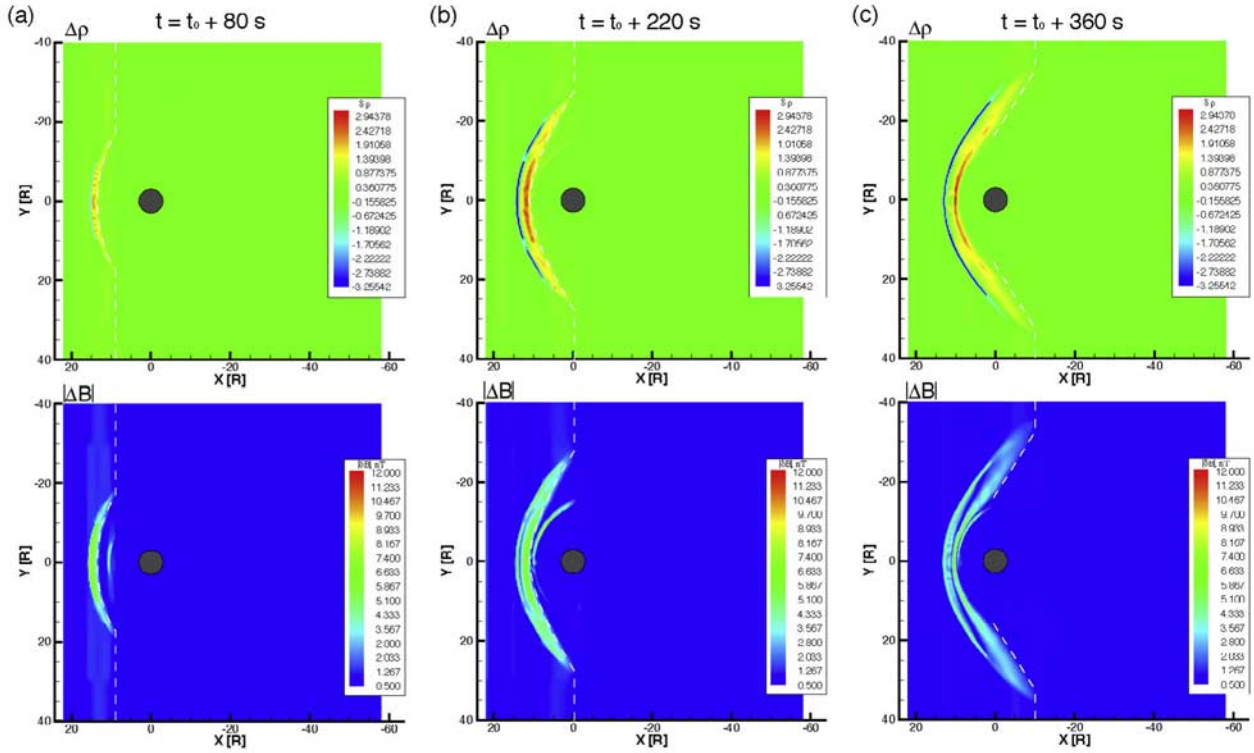

Figure 12. Spatial distributions of $\Delta\rho$ and ΔB in the X-Y plane (the Sun to the left and dawn to the bottom) obtained by our 3-D MHD simulation of the density-increase discontinuity. The circle in the middle is the inner boundary of the simulation. White dashed lines are drawn at the leading edge of the discontinuity. See text for details.

tosphere are given by, e.g., *Kabin et al.* [2003] and *Watanabe et al.* [2005].

[51] The inner boundary conditions are imposed at 3 R_E and represent magnetosphere-ionosphere coupling. Field-aligned currents calculated in the inner magnetosphere at 4 R_E are mapped into the ionosphere, where the electric potential is determined and then mapped back to the inner magnetosphere at 3 R_E under the assumption that the magnetic field lines are equipotentials. The convection velocity at the inner boundary is calculated from the mapped electric potential.

[52] The upstream outer boundary is positioned at 22 R_E. For the present simulation, the upstream conditions are obtained in the following way. The magnetic field data obtained by Wind are linearly interpolated to the same time points as the plasma data from Wind. The X component of the magnetic field is set to the constant value roughly averaged over the considered interval, in order to avoid introducing divergence of the magnetic field into the simulation domain. We assume that the normal of the discontinuities is aligned with the Sun-Earth line and that the solar wind is exactly along the Sun-Earth line (i.e., $v_y = v_z = 0$).

5.2.1. Density-Increase Discontinuity

[53] This section presents the results of the MHD simulation for the density-increase discontinuity. Figure 12 shows spatial distributions of $\Delta\rho$ (top) and $|\Delta B|$ (bottom) in the X-Y plane in GSM coordinates (the Sun to the left and dusk to the bottom), where $\Delta\rho$ is the difference in mass density between the solution at present time and 20 s ago; $|\Delta B|$ is, similarly, the absolute value of the change in $|B|$ over a 20 s interval. We make plots of the time differences of the solution, rather than the solution itself, because this representation removes the background variation of the MHD variables and shows the evolution of the disturbance much more clearly. The circle in the middle is the inner boundary of the simulation. The Wind data interval used as input is 1120–1205 UT. IMF B_x is set to -1.5 nT. White dashed lines are drawn at the leading edge of the discontinuity.

[54] Figure 12a corresponds to $t = t_0 + 80$ s, where t_0 is the time when the discontinuity first interacts with the nose of the bow shock. The density increases (yellow arc) in the discontinuity in the dayside magnetosheath. A density decrease (blue arc) behind (sunward of) the discontinuity indicates that the bow shock moves earthward; magnetosheath plasma is replaced by less dense pre-bow shock solar wind plasma. $|B|$ also changes in the discontinuity. Another $|B|$ increase is clearly seen around the magnetopause, where the discontinuity has not yet arrived. This is probably due to the earthward motion of the magnetopause caused by the fast shock (or fast waves) that is generated at the bow shock and propagates ahead of the discontinuity. We checked ΔB distributions between $t = t_0$ and $t = t_0 + 80$ s (not shown here), and found the $|B|$ increase indeed propagates ahead of the main discontinuity. Figures 12b and 12c correspond to $t = t_0 + 220$ s and $t = t_0 + 360$ s, respectively. The results including Figure 12a clearly show that the discontinuity is deformed into a concave shape in the magnetosheath although it is assumed to be straight in the solar wind, in agreement with the earlier simulations [e.g., *Šafránková*

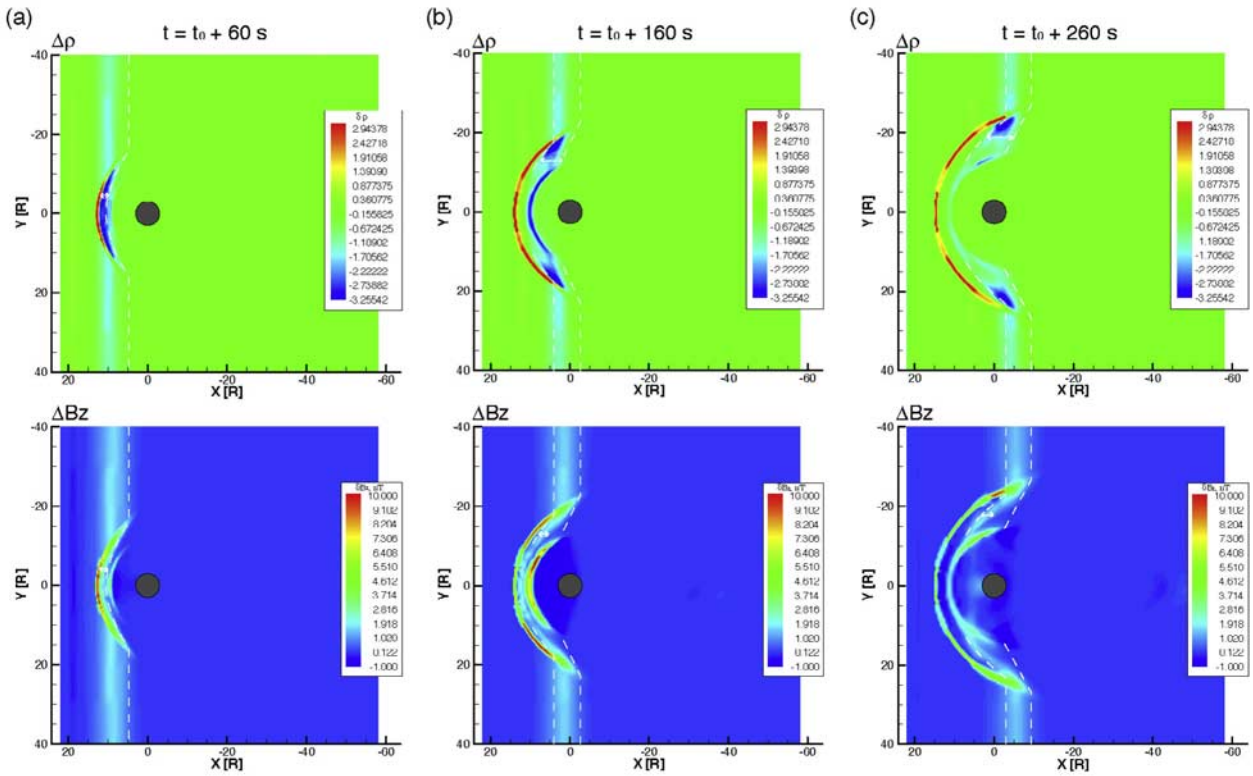

Figure 13. Spatial distributions of $\Delta\rho$ and ΔB_z in the X-Y plane, obtained by our 3-D MHD simulation of the density-decrease discontinuity, in the same format as Figure 12. White dashed lines are drawn at the leading and trailing edges of the discontinuity. White arrows indicate the spatial width of the $\Delta\rho$ and ΔB_z changes. See text for details.

et al., 2007]. The bow shock earthward speed was estimated to be ~150 km/s on the Sun-Earth line.

5.2.2. Density-Decrease Discontinuity

[55] Figure 13 shows spatial distributions of $\Delta\rho$ (top) and ΔB_z (bottom) for the density-decrease discontinuity in the same format as Figure 12, where ΔB_z is the difference in the Z component of the magnetic field during a 20 s interval. The Wind data interval used as input is 0905–1005 UT. IMF B_x is set to −0.25 nT. White dashed lines are drawn at the leading and trailing edges of the discontinuity.

[56] Figure 13a corresponds to $t = t_0 + 60$ s, where t_0 is the time when the discontinuity first interacts with the nose of the bow shock. The density decreases (blue arc) in the discontinuity in the dayside magnetosheath. A density increase (red curve) behind (sunward of) the discontinuity indicates that the bow shock moves sunward; solar wind plasma is replaced by denser magnetosheath plasma. B_z increases across the discontinuity. Another B_z increase is seen around the magnetopause before the discontinuity reaches there. The disturbances are likely associated with rarefaction waves launched at the bow shock by the interaction between the discontinuity and the bow shock.

[57] Figure 13b corresponds to $t = t_0 + 160$ s. The discontinuity lies in the dayside flank. White arrows indicate the spatial width of the change in each quantity. ρ decreases across the discontinuity. B_z increases across the discontinuity; the increase is concentrated near the trailing edge of the discontinuity although in the solar wind it is distributed over the discontinuity. A density decrease (blue arc, Figure 13b, top) and a B_z increase (red/yellow arc, Figure 13b, bottom) along the magnetopause indicate that the magnetopause moves sunward; magnetosheath plasma and magnetic field are replaced by less dense magnetospheric plasma and stronger magnetic field, respectively. Figure 13c corresponds to $t = t_0 + 260$ s. The spatial width of the density decrease in the discontinuity is wider than that at $t = t_0 + 160$ s, and the B_z increase is concentrated near the trailing edge.

[58] The simulation results clearly show that the discontinuity is deformed and assumes a concave shape in the magnetosheath although it was taken to have a planar front in the solar wind. The spatial width of the discontinuity (i.e., the ρ decrease) becomes wider as it propagates in the magnetosheath. A B_z increase appears near the trailing edge of the discontinuity. The bow shock sunward speed on the Sun-Earth line was estimated to be ~100 km/s between $t = t_0 + 60$ s and $t = t_0 + 160$ s and ~40 km/s between $t = t_0 + 160$ s and $t = t_0 + 260$ s.

6. Discussion

[59] The multipoint observations in the magnetosheath revealed the deformation and evolution of the discontinuities. In this section, we discuss how the disconti-

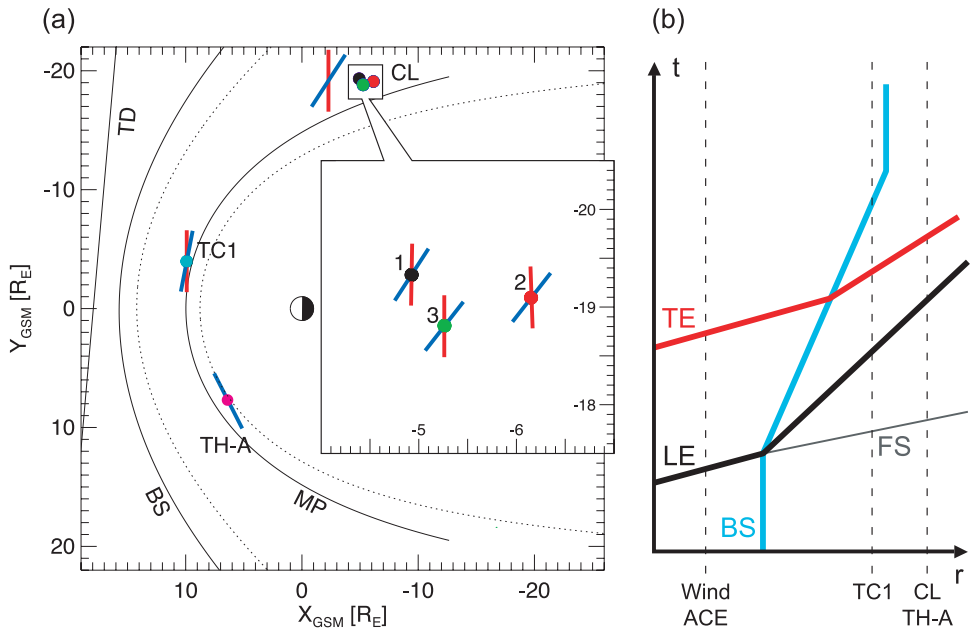

Figure 14. (a) Summary of the deformation of the fast forward shock and the density-increase discontinuity in the magnetosheath. CL and TH-A denote Cluster and THEMIS A, respectively. Red and blue bars represent the shock and discontinuity fronts obtained from the observations (see section 3.3 for details). TD denotes a tangential discontinuity. The bow shock (BS) and the magnetopause (MP) are drawn in the same way as in Figure 1. (b) An illustration of propagation of the leading edge (LE; black line) and the trailing edge (TE; red line) of the discontinuity, the bow shock (BS; light blue line), and the fast forward shock generated at the bow shock (FS; thin black line). Vertical dashed lines indicate positions of the spacecraft used in the present study. They qualitatively represent the observations of the discontinuity and/or the shock(s) by the spacecraft (see text for details).

nuities deform and what caused them to evolve in the magnetosheath.

6.1. Density-Increase Discontinuity

6.1.1. Deformation

[60] The observations showed that the forward fast shock was generated at the bow shock and propagated ahead of the density-increase discontinuity in the magnetosheath. The normal vector was almost aligned with the Sun-Earth line, being almost the same as that of the discontinuity in the interplanetary space. This implies that the fast shock propagates with the speed comparable to the discontinuity in the interplanetary space. This is consistent with *Völk and Auer* [1974], who demonstrated that the fast shock speed is 315.1 km/s when the incident solar wind flows at 287.7 km/s and the ratio of downstream to upstream density of a discontinuity is 2. *Wu et al.* [1993] showed in their theoretical analysis based on the R-H equations that the fast shock speed is comparable to the incident solar wind speed.

[61] The discontinuity front in the magnetosheath was inclined toward dusk on the dawnside and toward dawn on the duskside. The deformation was also presented by our MHD simulations. There are two reasons for the deformation: differences in the bow shock strength (as defined, for example, by the compression ratio for the plasma density, ε) along the bow shock surface and differences in travel distance. The bow shock is stronger near the subsolar point than around the flank. The solar wind is more decelerated across the bow shock near the subsolar point. It is slowed down less around the flanks. In addition, the solar wind can travel in the interplanetary space longer around the flanks, because the bow shock is literally shaped like a "bow" shape. Therefore, the discontinuity travels faster around the flank, undergoing the deformation in the magnetosheath. Figure 14a summarizes the observations of the deformation.

6.1.2. Evolution

[62] The observations showed differences in the duration of the discontinuity among spacecraft. The duration was 60 s at TC1 in the magnetosheath near noon, 65 s at THEMIS A in the dayside magnetosheath on the duskside, and 40–45 s at Cluster in the nightside and dawnside magnetosheath; it became shorter as the discontinuity propagated in the magnetosheath. The different durations arise from the different spatial width of the discontinuity, since the solar wind speed is virtually unchanged between the locations of the spacecraft. The discontinuity spatial width continued to narrow as the discontinuity propagated in the magnetosheath.

[63] We conclude that the observed compression of the discontinuity is due to bow shock earthward motion caused by the impact of the discontinuity on the bow shock. The bow shock is pushed toward the Earth when it is hit by a discontinuity with enhanced density (dynamic pressure) [e.g., *Völk and Auer*, 1974], as also demonstrated by our MHD simulation. At the earthward moving bow shock, the solar wind is less decelerated than at the stationary bow shock, as demonstrated by the theoretical analysis based on the R-H equations (see section 5). This causes the solar

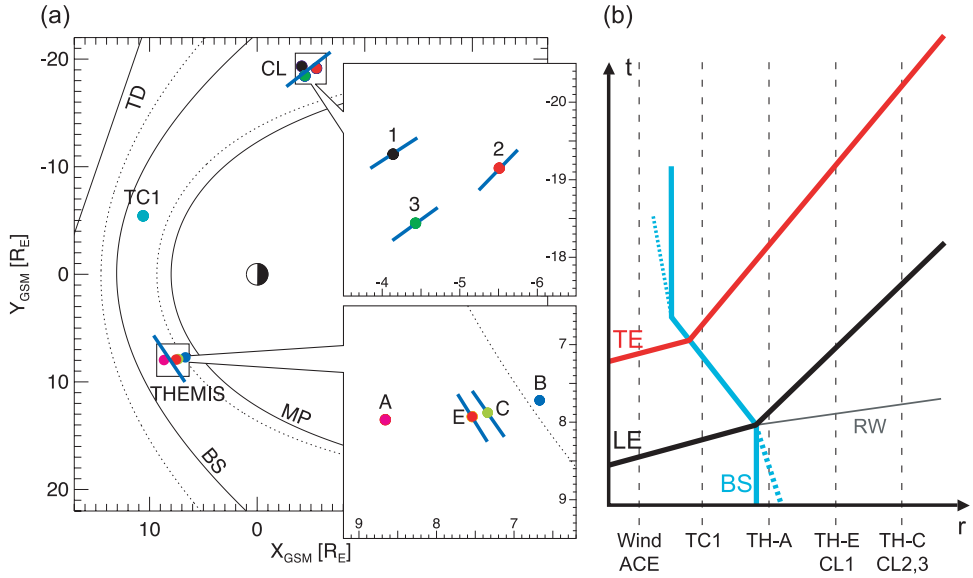

Figure 15. (a) Summary of the deformation of the density-decrease discontinuity in the magnetosheath. CL denotes Cluster. Blue bars represent the discontinuity front obtained from the observations (see section 4.3 for details). TD denotes a tangential discontinuity. The bow shock (BS) and the magnetopause (MP) are drawn in the same way as in Figure 5. (b) An illustration of propagation of the leading (black line) and trailing (red line) edges of the discontinuity, the bow shock (BS; light blue line), and the front of the rarefaction waves launched at the bow shock (RW; thin black line). A dotted light blue line represents the sunward moving bow shock before and after the arrival of the discontinuity at the bow shock. Vertical dashed lines represent positions of the spacecraft used in the present study. They qualitatively represent the observations of the discontinuity and/or the bow shock by the spacecraft (see text for details).

wind downstream of the bow shock to flow faster inside the discontinuity than at its leading edge. Thus the discontinuity keeps compressed as it propagates.

[64] Figure 14b illustrates the propagation of the fast forward shock (thin black line), the leading and trailing edge of the discontinuity (black and red lines), and the motion of the bow shock (light blue line). Vertical dashed lines qualitatively represent the observations of the discontinuity and/or the shock(s) by the spacecraft used in the present study. When we make comparisons between lines denoted by "TC1" and "CL/TH-A," the duration of discontinuity observations shortens as the discontinuity propagates. This interpretation is based on the assumption that the bow shock keeps moving after the trailing edge passes by the bow shock. This assumption is further supported for the examined event by the fact that TC1 crossed the bow shock after it observed the trailing edge (see Figure 3), as shown by the line denoted by TC1.

6.2. Density-Decrease Discontinuity

6.2.1. Deformation

[65] The observations indicated that the front of the density-decrease discontinuity was inclined toward dusk on the dawnside and toward dawn on the duskside. The deformation was also shown in our MHD simulation. We believe that the reasons for the deformation are the same as mentioned in section 6.1.1. Figure 15a summarizes the observations of the deformation.

6.2.2. Evolution

[66] The duration of observations of the discontinuity was 6.5–8.5 min at THEMIS and 9.5–10 min at Cluster in the magnetosheath, being longer at spacecraft further away from the bow shock. The different durations arise from the different spatial width of the discontinuity, since the solar wind speed is virtually unchanged between the locations of the spacecraft. The discontinuity spatial width continued to broaden as the discontinuity propagated in the magnetosheath.

[67] We conclude that the observed expansion of the discontinuity is due to a start or enhancement of the bow shock sunward motion caused by the impact of the discontinuity on the bow shock. The bow shock moves toward the Sun when it is hit by a discontinuity across which the density decreases [e.g., *Völk and Auer*, 1974], as also demonstrated by our MHD simulation. The solar wind is more decelerated at the sunward moving bow shock, as demonstrated by the theoretical analysis based on the R-H equations (see section 5). Downstream of the bow shock, plasma inside the discontinuity flows slower than the leading edge, as confirmed by plasma velocity data obtained by THEMIS and Cluster (see Figures 8 and 9). Thus, the discontinuity keeps expanded as it propagates in the magnetosheath.

[68] Figure 15b illustrates the propagation of the leading edge (black line), the trailing edge of the discontinuity (red line), and the rarefaction wave (thin black line). Vertical dashed lines qualitatively represent the observations of the discontinuity and/or the bow shock by the spacecraft used in the present study. When we make comparisons between lines denoted by "TH-A," "TH-E/CL1," and "THC/CL2,3," observations of the discontinuity become longer as it propagates in the magnetosheath. This interpretation is

based on the assumption that the bow shock keeps moving after the trailing edge passes by the bow shock. Although we cannot infer the bow shock speed and its changes quantitatively from the observations available, we believe that the assumptions are qualitatively valid, because the MHD simulation demonstrates that the bow shock is moving sunward after the whole discontinuity passed by the bow shock (see red/orange arc in Figure 13c, top).

[69] Another noteworthy feature is the steepening of a B_z reversal at the trailing edge of the discontinuity (~1016–~1021 UT at THEMIS A, ~1020–~1024 UT at THEMIS E, ~1024–~1025 UT at THEMIS C, ~1017–1024 UT at Cluster 1, and ~1023–~1025 UT at Cluster 3 and 2). The reversal becomes faster as the discontinuity propagated in the magnetosheath. The MHD simulation demonstrated that while B_z is changed gradually in the solar wind, a steep B_z increase appears near the trailing edge in the magnetosheath. We interpret this steepening as a consequence of the compression of the discontinuity trailing edge by fast solar wind flows following the discontinuity. Cluster and THEMIS observations (Figures 8 and 9) confirmed that the solar wind was faster near the trailing edge than inside the discontinuity. The interpretation is also supported by the fact that the spacecraft observing a steep B_z reversal (THEMIS C and E and Cluster 1, 2, and 3) saw an overshoot of $|B|$ indicating the compression of the magnetic field, which was not seen by the spacecraft observing a gradual B_z reversal (DSP/TC1 and THEMIS A).

[70] The fast solar wind flows is likely due to the slowing down or stopping of the sunward motion of the bow shock after the whole discontinuity passed by the bow shock. Since the Alfvén and sonic Mach numbers remained constant behind the discontinuity, the bow shock should stop at a new equilibrium position. The bow shock stopping in the rest frame is regarded as the earthward speed up of the bow shock in the frame of the sunward moving bow shock. We have shown that downstream plasma speed (i.e., in the magnetosheath) becomes faster when the bow shock moves earthward. It is highly probably that the slowing down or stopping of the sunward moving bow shock causes fast solar wind flows behind the discontinuity.

7. Summary and Conclusions

[71] The present study examined the interactions of solar wind discontinuities accompanied by density changes with the bow shock, using multipoint observations in the magnetosheath by THEMIS, Cluster, and DSP/TC1. We focused on their deformation and evolution in the magnetosheath.

[72] A discontinuity, across which the density increases and the magnetic field decreases, arrived near the bow shock at about 1245 UT on 21 June 2007. The spacecraft in the magnetosheath observed the fast forward shock generated at the bow shock as well as the discontinuity transmitted across the bow shock. We estimated the normal direction of the shock and discontinuity, and then confirmed that the shock front propagated with the normal similar to the incident discontinuity and that the discontinuity was deformed into a concave shape (i.e., tilted toward dusk on the dawnside and toward dawn on the duskside). The discontinuity was being compressed as it propagated in the magnetosheath. We suggest that bow shock antisunward motion is responsible for the compression. The motion is caused by an impact of the discontinuity on the bow shock.

[73] Another discontinuity, across which the density decreases and the magnetic field increases, arrived near the bow shock at about 1010 UT on 21 June 2007. The spacecraft in the magnetosheath observed the transmitted discontinuity, which we confirmed was deformed into a concave shape. As the discontinuity propagated in the magnetosheath, it was being expanded. We conclude that the sunward motion of the bow shock (or speeding-up of the sunward motion) is responsible for the expansion. The motion is caused by the impact of the discontinuity on the bow shock. Near the trailing edge of the discontinuity, a B_z increase became steeper, accompanied by an overshoot of $|B|$. We suggest that the trailing edge was compressed by the solar wind flow behind it with faster speed. The faster flow may be due to the stopping or slowing down of the sunward bow shock motion.

[74] **Acknowledgments.** Wind and ACE data are provided by Coordinated Data Analysis Web (CDAWeb), NASA. We are grateful to H. Eichelberger and G. Laky for helping with the Cluster and Double Star data analysis. We thank A. Retinò for his helpful comments. THEMIS was made possible and is supported in the United States by NASA NAS5-02099. The work of the IGEP team at the Technical University of Braunschweig was financially supported by the German Ministerium für Wirtschaft und Technologie and the German Zentrum für Luft- und Raumfahrt under grant 50QP0402. K. Kabin and R. Rankin are supported by the Canadian Space Agency. Figures 14 and 15 are drawn by Mayuko Keika.

[75] Zuyin Pu thanks Andrey A. Samsonov and the other reviewers for their assistance in evaluating this paper.

References

Angelopoulos, V. (2008), The THEMIS mission, *Space Sci. Rev.*, *141*, 5–34, doi:10.1007/s11214-008-9336-1.

Auster, H. U., et al. (2008), The THEMIS fluxgate magnetometer, *Space Sci. Rev.*, *141*, 235–264, doi:10.1007/s11214-008-9365-9.

Balogh, A., et al. (2001), The Cluster magnetic field investigation: Overview of in-flight performance and initial results, *Ann. Geophys.*, *19*, 1207–1217.

Baumjohann, W., and R. A. Treumann (1996), *Basic Space Plasma Physics*, Imperial Coll. Press, London.

Cable, S., and Y. Lin (1998), Three-dimensional MHD simulations of interplanetary rotational discontinuities impacting the Earth's bow shock and magnetosheath, *J. Geophys. Res.*, *103*, 29,551–29,567, doi:10.1029/1998JA900025.

Carr, C., et al. (2005), The Double Star magnetic field investigation: Instrument design, performance and highlights of the first year's observations, *Ann. Geophys.*, *23*, 2713–2732.

Colburn, D. S., and C. P. Sonett (1966), Discontinuities in the solar wind, *Space Sci. Rev.*, *5*, 439–506, doi:10.1007/BF00240575.

Farrugia, C. J., N. V. Erkaev, U. Taubenschuss, V. A. Shaidurov, C. W. Smith, and H. K. Biernat (2008), A slow mode transition region adjoining the front boundary of a magnetic cloud as a relic of a convected solar wind feature: Observations and MHD simulation, *J. Geophys. Res.*, *113*, A00B01, doi:10.1029/2007JA012953.

Harvey, C. C. (1998), Spatial gradients and the volumetric tensor, in *Analysis Methods for Multi-spacecraft Data*, edited by G. Paschmann and P. W. Daly, Eur. Space Agency Spec. Publ., *ESA SP-449*, 307–348.

Kabin, K. (2001), A note on the compression ratio in MHD shocks, *J. Plasma Phys.*, *66*, 259–274, doi:10.1017/S0022377801001295.

Kabin, K., R. Rankin, R. Marchand, T. I. Gombosi, C. R. Clauer, A. J. Ridley, V. O. Papitashvili, and D. L. DeZeeuw (2003), Dynamic response of Earth's magnetosphere to B_y reversals, *J. Geophys. Res.*, *108*(A3), 1132, doi:10.1029/2002JA009480.

Klein, L. W., and L. F. Burlaga (1982), Interplanetary magnetic clouds at 1 AU, *J. Geophys. Res.*, *87*, 613–624, doi:10.1029/JA087iA02p00613.

Koval, A., J. Šafránková, Z. Němeček, L. Přech, A. A. Samsonov, and J. D. Richardson (2005), Deformation of interplanetary shock fronts in the

magnetosheath, *Geophys. Res. Lett.*, *32*, L15101, doi:10.1029/2005GL023009.

Lepping, R. L., and P. D. Argentiero (1971), Single spacecraft method of estimating shock normals, *J. Geophys. Res.*, *76*, 4349–4359, doi:10.1029/JA076i019p04349.

Lepping, R. P., et al. (1995), The Wind magnetic-field investigation, *Space Sci. Rev.*, *71*, 207–229, doi:10.1007/BF00751330.

Lepping, R. L., A. Szabo, K. W. Ogilvie, and R. J. Fitzenreiter (1996), Magnetic cloud-bow shock interaction: Wind and IMP-8 observations, *Geophys. Res. Lett.*, *23*, 1195–1198, doi:10.1029/96GL01287.

Lin, R. P., et al. (1995), A 3-dimensional plasma and energetic particle investigation for the Wind spacecraft, *Space Sci. Rev.*, *71*, 125–153, doi:10.1007/BF00751328.

Maynard, N. C., et al. (2007), Interaction of the bow shock with a tangential discontinuity and solar wind density decrease: Observations of predicted fast mode waves and magnetosheath merging, *J. Geophys. Res.*, *112*, A12219, doi:10.1029/2007JA012293.

Maynard, N. C., C. J. Farrugia, D. M. Ober, W. J. Burke, M. Dunlop, F. S. Mozer, H. Rème, P. Décréau, and K. D. Siebert (2008), Cluster observations of fast shocks in the magnetosheath launched as a tangential discontinuity with a pressure increase crossed the bow shock, *J. Geophys. Res.*, *113*, A10212, doi:10.1029/2008JA013121.

McFadden, J. P., C. W. Carlson, D. Larson, V. Angelopoulos, M. Ludlam, R. Abiad, and B. Elliot (2008), The THEMIS ESA plasma instrument and in-flight calibration, *Space Sci. Rev.*, *141*, 277–302, doi:10.1007/s11214-008-9440-2.

Neubauer, F. M. (1975), Nonlinear oblique interaction of interplanetary tangential discontinuities with magnetogasdynamic shocks, *J. Geophys. Res.*, *80*, 1213–1222, doi:10.1029/JA080i010p01213.

Neugebauer, M. (2006), Comment on the abundances of rotational and tangential discontinuities in the solar wind, *J. Geophys. Res.*, *111*, A04103, doi:10.1029/2005JA011497.

Neugebauer, M., D. R. Clay, B. E. Goldstein, B. T. Tsurutani, and R. D. Zwickl (1984), A reexamination of rotational and tangential discontinuities in the solar wind, *J. Geophys. Res.*, *89*, 5395–5408, doi:10.1029/JA089iA07p05395.

Peredo, M., J. A. Slavin, E. Mazur, and S. A. Curtis (1995), Three-dimensional position and shape of the bow shock and their variation with Alfvénic, sonic and magnetosonic Mach numbers and interplanetary magnetic field orientation, *J. Geophys. Res.*, *100*, 7907–7916, doi:10.1029/94JA02545.

Petrinec, S. M., and C. T. Russell (1997), Hydrodynamic and MHD equations across the bow shock and along the surfaces of planetary obstacles, *Space Sci. Rev.*, *79*, 757–791, doi:10.1023/A:1004938724300.

Powell, K. G., P. L. Roe, T. J. Linde, T. I. Gombosi, and D. L. DeZeeuw (1999), A solution-adaptive upwind scheme for ideal magnetohydrodynamics, *J. Comput. Phys.*, *154*, 284–309, doi:10.1006/jcph.1999.6299.

Přech, L., Z. Němeček, and J. Šafránková (2008), Response of magnetospheric boundaries to the interplanetary shock: Themis contribution, *Geophys. Res. Lett.*, *35*, L17S02, doi:10.1029/2008GL033593.

Rème, H., et al. (2001), First multispacecraft ion measurements in and near the Earth's magnetosphere with the identical Cluster ion spectrometry (CIS) experiment, *Ann. Geophys.*, *19*, 1303–1354.

Russell, C. T., M. M. Mellott, E. J. Smith, and J. H. King (1983), Multiple spacecraft observations of interplanetary shocks: Four spacecraft determination of shock normals, *J. Geophys. Res.*, *88*, 4739–4748, doi:10.1029/JA088iA06p04739.

Šafránková, J., Z. Němeček, L. Přech, A. A. Samsonov, A. Koval, and K. Andréeová (2007), Modification of interplanetary shocks near the bow shock and through the magnetosheath, *J. Geophys. Res.*, *112*, A08212, doi:10.1029/2007JA012503.

Samsonov, A. A., Z. Němeček, and J. Šafránková (2006), Numerical MHD modeling of propagation of interplanetary shock through the magnetosheath, *J. Geophys. Res.*, *111*, A08210, doi:10.1029/2005JA011537.

Samsonov, A. A., D. G. Sibeck, and J. Imber (2007), MHD simulation for the interaction of an interplanetary shock with the Earth's magnetosphere, *J. Geophys. Res.*, *112*, A12220, doi:10.1029/2007JA012627.

Shue, J. H., et al. (1998), Magnetopause location under extreme solar wind conditions, *J. Geophys. Res.*, *103*, 17,691–17,700, doi:10.1029/98JA01103.

Smith, C. W., J. L'Heureux, N. F. Ness, M. Acuña, L. F. Burlaga, and J. Scheifele (1998), The ACE magnetic fields experiment, *Space Sci. Rev.*, *86*, 613–632, doi:10.1023/A:1005092216668.

Song, P., and C. T. Russell (1999), Time series data analyses in space physics, *Space Sci. Rev.*, *87*, 387–463, doi:10.1023/A:1005035800454.

Sonnerup, B. U. Ö., and J. L. J. Cahill (1967), Magnetopause structure and attitude from Explorer 12 observations, *J. Geophys. Res.*, *72*, 171–183, doi:10.1029/JZ072i001p00171.

Sonnerup, B. U. Ö., and M. Scheible (1998), Minimum and maximum variance analysis, in *Analysis Methods for Multi-spacecraft Data*, edited by G. Paschmann and P. W. Daly, *Eur. Space Agency Spec. Publ.*, *ESA SP-449*, 185–220.

Tóth, G., et al. (2005), Space weather modeling framework: A new tool for the space science community, *J. Geophys. Res.*, *110*, A12226, doi:10.1029/2005JA011126.

Verigin, M., G. Kotova, A. Szabo, J. Slavin, T. Gombosi, K. Kabin, F. Shugaev, and A. Kalinchenko (2001), Wind observations of the terrestrial bow shock: 3-D shape and motion, *Earth Planets Space*, *53*, 1001–1009.

Völk, H. J., and R. D. Auer (1974), Motions of the bow shock induced by interplanetary disturbances, *J. Geophys. Res.*, *79*, 40–48, doi:10.1029/JA079i001p00040.

Watanabe, M., K. Kabin, G. J. Sofko, R. Rankin, T. I. Gombosi, A. J. Ridley, and C. R. Clauer (2005), Internal reconnection for northward interplanetary magnetic field, *J. Geophys. Res.*, *110*, A06210, doi:10.1029/2004JA010832.

Wei, F. S., X. Feng, F. Yang, and D. Zhong (2006), A new non-pressure-balanced structure in interplanetary space: Boundary layers of magnetic clouds, *J. Geophys. Res.*, *111*, A03102, doi:10.1029/2005JA011272.

Wu, B. H., M. E. Mandt, L. C. Lee, and J. K. Chao (1993), Magnetospheric response to solar wind dynamic pressure variations: Interaction of interplanetary tangential discontinuities with the bow shock, *J. Geophys. Res.*, *98*, 21,297–21,311, doi:10.1029/93JA01013.

V. Angelopoulos, Institute of Geophysics and Planetary Physics, University of California, Box 951567, 2712 Geology Building, Los Angeles, CA 90095-1567, USA.

H. U. Auster, K. H. Fornaçon, and K. H. Glassmeier, Institut für Geophysik und extraterrestrische Physik, Technische Universität Braunschweig, Mendelssohnstrasse 3, D-38106 Braunschweig, Germany.

W. Baumjohann, K. Keika, W. Magnes, and R. Nakamura, Space Research Institute, Austrian Academy of Sciences, Schmiedlstrasse 6, A-8042 Graz, Austria. (kunihiro.keika@oeaw.ac.at)

C. W. Carlson and J. P. McFadden, Space Sciences Laboratory, University of California, 7 Gauss Way, Berkeley, CA 94720-7450, USA.

C. M. Carr and E. A. Lucek, Space and Atmospheric Physics Group, Imperial College London, South Kensington Campus, London SW7 2AZ, UK.

I. Dandouras, Centre d'Etude Spatiale des Rayonnements, Université Paul Sabatier, UMR 5187, CNRS, 9 Avenue du Colonel Roche, F-31028 Toulouse CEDEX 4, France.

K. Kabin and R. Rankin, Department of Physics, University of Alberta, Edmonton, AB T6G 2J1, Canada.

D. G. Sibeck, NASA Goddard Space Flight Center, 8800 Greenbelt Road, Greenbelt, MD 20771, USA.